

Master's Thesis

Untersuchung der Bindungsdynamik von prolinreichen antimikrobiellen Peptiden Api88 und Api137 durch Molekulardynamik-Simulationen

Exploring the Binding Dynamics of Proline-Rich Antimicrobial Peptides Api88 and Api137 through Molecular Dynamics Simulations

prepared by

Ole Berendes

at the Max Planck Institute for Multidisciplinary Sciences – Department for Theoretical
and Computational Biophysics

Date of Submission: 20th May 2024

Supervisors: Dr. Lars V. Bock, Sara Gabrielli

First Referee: Prof. Dr. Helmut Grubmüller

Second Referee: Prof. Dr. Martin Zacharias

Preface

Parts of the results of this thesis have been published in Lauer et al. [1].

Abstract

Synthetic antimicrobial peptides Api137 and Api88 are promising lead compounds in antimicrobial research. They share the same sequence, apart from the C-terminus, which is amidated in Api88. Although they both suppress protein synthesis by binding to the peptide exit tunnel (PET) of the ribosome, recent cryo-EM data suggest that they act by different mechanisms. Api137 traps release factors and prevents dissociation of the peptide chain. Api88 binds to the same sites as Api137 but is more deeply positioned into the tunnel, and the cryo-EM density is less defined. The less defined cryo-EM density of Api88 can be tentatively modelled by three different conformations.

The conformational diversity of Api88 gives rise to various questions regarding its binding dynamics. In this work, I examined whether the three Api88 conformations represent metastable states and how much density information can be attributed to each conformation. Further, I tried to improve the explanation of the density with structures predicted by MD simulations. Lastly, I compared the binding dynamics of of Api88 to Api137 and investigated how the chemical differences between the two peptides affect their flexibility when bound in the exit tunnel.

To address these key questions, I performed all-atom MD simulations starting from the three modelled conformations of Api88, Api137 and an amidated version of Api137 with the same coordinates in the PET. The results suggest that Api88 adopts metastable conformational states. To estimate the contribution of the modelled conformations to the overall conformational ensemble, I computed cryo-EM density maps from the MD ensembles of each state. After that, I combined the computed maps and optimised the weights of the states to maximise the correlation with the experimental map. The optimally weighted MD ensemble displayed an improved correlation to the experimental map compared to the optimally weighted initial conformations suggesting that the dynamics of the peptide observed in the experiment is captured by the MD simulations. Additionally, I identified a minimal number of MD structures sufficient to describe the ensemble. The analysis further shows that one of the three initially modelled conformations contributes most to the cryo-EM density. Compared to the other two structures, it shows a slight shift toward the peptidyl transferase centre at the tunnel's beginning. In comparison, the modified Api137 exhibits more rigid binding dynamics than Api88. This effect can be traced back to the chemical modifications in its C-terminal residue.

Contents

1. Introduction	1
2. Background	5
2.1. Structure and function of the bacterial ribosome	5
2.2. Proline-rich antimicrobial peptides	8
2.3. Mechanisms of Api88 and Api137	8
2.4. Cryogenic electron microscopy	9
2.5. Molecular dynamics simulations	12
2.5.1. The MD algorithm	12
2.5.2. Solvent treatment	14
2.5.3. Calculation of long-range electrostatic interactions	14
2.5.4. Temperature and pressure coupling	14
2.6. Principal component analysis	16
2.7. Computation of density maps from atomic models	17
2.8. Root mean square deviation	17
2.9. Root mean square fluctuation	18
2.10. Pearson correlation coefficient	18
2.11. Bootstrapping	19
3. Methods	21
3.1. Simulation Setup	21
3.1.1. System preparation and energy minimisation	21
3.1.2. Solvent equilibration	23
3.1.3. Release of position restraints	23
3.2. Post-processing of simulation trajectories	24
3.3. Principal component analysis	24
3.4. Calculating cryo-EM maps from MD snapshots	25
3.5. Quantifying the contributions of Api88 conformations to the cryo-EM density	25

Contents

3.6. Finding optimal MD structures	26
4. Results and discussion	27
4.1. Principal component analysis of Api88 trajectories	27
4.2. Contributions of Api88 conformations to the cryo-EM density	29
4.3. Improving explanation of cryo-EM data with MD-generated conformations	31
4.4. Influence of the C-terminus on binding dynamics of Api88 and Api137 .	31
5. Conclusions and outlook	39
Bibliography	41
A. PCA of Api88 trajectories	47
B. PCA of Api137 trajectories	49
C. PCA of combined Api88 and Api137 trajectories	51

1. Introduction

Antimicrobial resistance poses a significant global health threat. Although some bacterial resistance mutations are as old as 30 000 years [2], increased use of antibiotics in the last decades puts pathogens under high evolutionary pressure and drives the development of drug-resistant bacteria. The rising resistance level necessitates the exploration of novel therapeutic strategies such as antimicrobial peptides (AMPs).

Antimicrobial peptides are genetically encoded and constitute a crucial component of the innate immune defence system in diverse species. Many antimicrobial peptides kill bacteria by dissolving their cellular membranes, while others target intracellular components [3].

Peptides belonging to the subclass of proline-rich AMPs (PrAMPs) use the latter mechanism [4]. As their name suggests, these peptides exhibit a high content of proline residues and arginines. They permeate the outer and inner bacterial membrane and appear to primarily target the ribosome [5–7], which serves as the protein factory of every living cell. The ribosome is the catalytic site for translating gene sequences in the form of messenger RNAs (mRNAs) to peptide chains of amino acids that can fold into proteins. PrAMPs are expressed in many insects and some species of mammals but have not been found in humans [4]. Thus, they present a promising avenue for developing antimicrobial drugs, which could fill a gap in our innate immune system.

This thesis focuses on two synthetic designer PrAMPs, Api88 and Api137, which stall protein translation at the bacterial ribosome and share great similarities in their amino acid sequence and binding sites. They are chemical derivatives of the naturally occurring PrAMP apidaecin 1b, which is found in western honey bees (*Apis mellifera*) [8]. The amino acid sequence of apidaecin 1b has been iteratively refined to achieve desired properties such as high efficacy in *in vivo* and *in vitro* experiments [9] and stability against degradation by bacteria [10]. Api88 and Api137 emerged as lead compounds due to their high antibacterial activity. Florin et al. [7] elucidated the antibacterial mechanism of Api137. The authors created an atomic model from a 3-dimensional density map obtained with cryogenic electron microscopy (cryo-EM). The model shows the binding

1. Introduction

position of Api137 in the ribosomal exit tunnel. The exit tunnel is a narrow space in the ribosome that hosts the nascent peptide chain during translation. The chain leaves the ribosome through the tunnel after the translation process is completed.

A more recent cryo-EM investigation of our collaborators in Christian Spahn's lab identified a similar binding site for Api88 [1]. In contrast to Api137, three models depicting different peptide conformations were needed to describe the cryo-EM density. The models from Christian Spahn's lab and the underlying density maps provide the foundation for this work. Lauer et al. [1] further identified previously unknown binding sites of Api88 and Api137 in the tunnel and other parts of the ribosome, which are not discussed here due to their very recent discovery.

Computational approaches like molecular dynamics (MD) simulations can complement experimental structural biology [11]. MD simulations add dynamic information to the static structure models. Starting from a single atomic model, an MD simulation solves the Newtonian equations of motion for each atom, thus generating a trajectory of structures that capture molecular motions on an atomic level and a temporal resolution of femtoseconds. Here, I will perform MD simulations starting from the cryo-EM structures of ribosome-bound Api88 and Api137 to address the following questions.

1. Do the three modelled conformations of Api88 represent metastable states, or can interconversions be observed on the simulation time scale?
2. The cryo-EM map of Api88 captures all three modelled conformations. How much does each conformation contribute to the density?
3. Can MD simulations predict alternative structures for Api88 that might describe the cryo-EM density better than the original models?
4. How do the binding dynamics of Api88 differ from those of Api137?

Each conformation of Api88 that was present in the cryo-EM sample contributes to the density, which, therefore, represents an ensemble of different conformations. Certain conformations might occur more frequently in the sample and contribute more to the cryo-EM density map. To quantify the contributions of each of the three modelled conformations, I computed density maps from the MD simulation data and compared them to the cryo-EM density maps.

I used principal component analysis (PCA) to assess the conformational space sampled by MD simulations of Api88 and to check the metastability of each of the three conformations on the order of the simulation time scale.

The simulation trajectories produced an enormous amount of possible conformations for Api88. I devised an algorithm that performed a guided search of the MD structures to identify a set of conformations providing a similar or better explanation of the cryo-EM map than the initial three models.

Lastly, it is interesting to compare the different binding dynamics of Api88 and Api137 since the only chemical difference between the two peptides is in their C-terminus (one end of the peptide chain), where Api88 carries a carboxamide (CONH₂) and Api137 a carboxylic acid (COOH). The fact that the Api88 density can only be described by an ensemble of three conformations of Api88 suggests a more flexible behaviour at its binding site in the exit tunnel compared to Api137. I used simulations of both peptides to further explore the effect of the C-terminal modification.

2. Background

2.1. Structure and function of the bacterial ribosome

A comprehensive overview of the structure and function of ribosomes can be found in Alberts [12], which was used as the source of information for the following section if not specified otherwise.

Ribosomes are macromolecular complexes that act as protein factories in eukaryotic and prokaryotic cells. An average *E. Coli* bacterium contains approximately 20 000 ribosomes [13]. Each ribosome is assembled from a small and a large subunit. The subunits are typically denoted by their sedimentation coefficient, measured in Svedberg units. In bacterial ribosomes, the small subunit has a coefficient of 30S, the large subunit 50S, and when assembled, the ribosome totals 70S. Ribosomal ribonucleic acid (rRNA), complemented by several ribosomal proteins, constitutes most of the ribosome. The ribosomal proteins are primarily located at the surface. Specifically, the bacterial 50S subunit includes two rRNAs (23S and 5S) and 31 ribosomal proteins, while the 30S subunit comprises the 16S rRNA and 21 proteins.

Protein translation is the process of producing proteins according to the genetic code, which is controlled and catalysed by the ribosome. Translation is a multistep process of initiation, elongation, and termination (Figure 2.1). It involves specific functional sites of the ribosome that span both subunits. During the translation process, the genetic information carried by the nucleotides in an mRNA strand is used to build a chain of amino acids, called peptide, that will later fold into the desired protein. The two termini of a peptide are called N- and C-terminus. The C-terminus is normally capped by a carboxylic acid, while the N-terminus is capped by an amide. The amino acid sequence of a peptide is always written in the direction from N- to C-terminus. Three consecutive mRNA nucleotides form a codon that can be decoded to one amino acid with the help of an adapter molecule called transfer RNA (tRNA). The ribosome contains three binding sites for tRNAs, the aminoacyl (A) site, the peptidyl (P) site and the exit (E) site. A specific type of tRNA carries a specific amino acid and contains an anticodon nucleotide triplet

2. Background

that can form complementary base-pairing interactions with its associated mRNA codon nucleotides.

The first step in the translation process is initiation, where the 70S ribosome is assembled around an mRNA strand. The two subunits are brought together with the help of initiation factors IF1, IF2, or IF3, resulting in the mRNA running along the subunit interface while being anchored to an mRNA binding site at the small subunit. At the same time, an fMet-tRNA is placed at the P site. The fMet-tRNA contains the anticodon for the start codon AUG, which marks the beginning of a protein-coding sequence on the mRNA and carries the corresponding amino acid N-formylmethionine.

New amino acids are iteratively added to the C-terminus of the nascent peptide chain during the elongation phase. The elongation factor EF-Tu delivers an aminoacylated tRNA to the A (accommodation) site at the beginning of an elongation step. If it carries the correct anticodon, it will bind tightly to the ribosome. Subsequently, the N-formylmethionine (first elongation step) or peptide chain (later elongation steps) detaches from the P-site tRNA and attaches to the amino acid at the A-site tRNA (transpeptidation). The ribosome acts as an enzyme and catalyses this peptidyl transferase reaction. The catalytic activity occurs in the peptidyl transferase centre (PTC) in the large subunit, at the CCA-tail of the P-site tRNA, where the peptide is bound. Further, the PTC marks the beginning of the peptide exit tunnel (PET), which provides the necessary space for the peptide chain to grow. Subsequently, the ribosome shifts by one codon in the reading direction along the mRNA strand while the two tRNAs stay in place (translocation). After translocation, the former P-site tRNA, which is now deacylated, resides at the E site, where it is ejected from the ribosome, while the former A-site tRNA holding the nascent chain has been transferred to the P site. The A site is now free to accommodate another aminoacylated tRNA for the next elongation step.

The elongation cycle continues until a stop codon is encountered, leading to the termination of the translation process. The stop codon is not recognised by a tRNA but rather by one of the release factors RF1, RF2, or RF3. These factors cleave the peptide chain from the P-site tRNA. The peptide leaves the ribosome through the exit tunnel. After that, the 70S ribosome is disassembled into its subunits, which can be reused in another translation process.

2.1. Structure and function of the bacterial ribosome

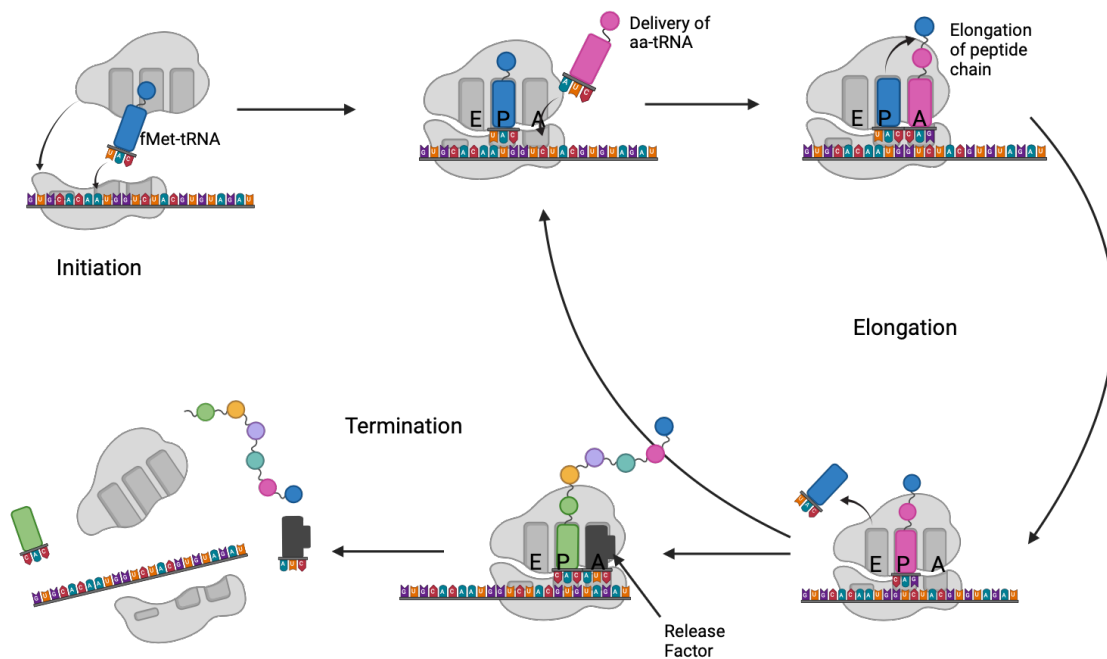


Figure 2.1.: Schematic overview of the translation process. During the initiation phase, the ribosome is assembled, and a fMet-tRNA (blue) binds to the P site. The nascent peptide chain is elongated by aminoacylated tRNAs (magenta) that bind to the A site and connect their carried residue to the chain. A release factor (black) cleaves the peptide chain and initiates the termination of the translation process.

2.2. Proline-rich antimicrobial peptides

Proline-rich antimicrobial peptides (PrAMPs) are integral components of the innate immune system found in arthropods and mammalian species [4]. The peptides are synthesised within immature phagocyte cells and stored in granules [14] as inactive precursors. Upon bacterial infection, phagocytes release the PrAMP-precursors into the extracellular space or sequester bacteria within phagosomes, subsequently merging them with PrAMP granules [15]. At the site of action, the inactive precursors undergo activation through proteolytic cleavage of the pre-and post-sequences that render them inert [15]. The membrane transporter SbmA transports activated PrAMPs into the bacterial cytoplasm [4].

PrAMPs exert their antimicrobial activity by binding inside the ribosomal exit tunnel. Initially, research suggested that the molecular chaperone DnaK was the primary target of PrAMPs [16]. DnaK is a heat shock protein that protects cells from thermal stress by catalysing the correct folding of freshly synthesised proteins. However, this model did not fully explain the effectiveness of PrAMPs against *E. Coli* strains that lack DnaK [5]. Subsequent research identified the ribosomal exit tunnel as the primary target of PrAMPs [7].

PrAMPs can be categorised into two classes based on their binding mode [4]. Oncocin-type PrAMPs, including oncocin and pyrrolicocin i. a., exhibit an inverted orientation within the peptide exit tunnel relative to the nascent peptide chain during translation, with their N-terminus reaching into the A site. These peptides occupy the A-site binding pocket, the A-site crevice, and the upper region of the peptide exit tunnel. In contrast, apidaecin-type PrAMPs, such as apidaecin 1b, Api88, and Api137, bind in the same direction as the nascent peptide chain, with their C-terminus oriented towards the A site. Unlike oncocin-type PrAMPs, apidaecins do not penetrate the A-site binding pocket.

2.3. Mechanisms of Api88 and Api137

The first detailed description of a termination-stalling mechanism of Api137 can be found in Florin et al. [7]. Api137 exerts its inhibitory effect on translation termination by trapping release factors at ribosomes, thus depleting the available factors needed to release peptide chains at other ribosomes. When a completed peptide chain leaves the ribosome, Api137 can enter the exit tunnel and bind to the release factor attached to the A site (Figure 2.2). This trapping of release factors initiates downstream effects that impede

protein production. Ribosomes directly stalled by Api137 cannot participate in subsequent translation rounds, but this affects only a limited subset of ribosomes. Given the relatively smaller pool of available release factors compared to the number of ribosomes, the translation machinery relies on a rapid turnover rate of these factors. At sufficiently high concentrations, Api137 effectively captures nearly all release factors. Consequently, Api137 stalls most active ribosomes by making them incapable of releasing their peptide chains due to a shortage of release factors. Florin et al. [7] further proposed that the resultant scarcity of free release-factors may increase stop-codon read-through, consequently inducing protein mistranslations. The inhibitory mechanism of Api88 is not yet understood.

Api88 and Api137 have nearly the same amino acid sequence. The only difference lies in the C-terminus. A carboxylic acid (Gu-ONNRPVYIPRPRPPHPRL-OH) caps Api137, while Api88 has an amide (Gu-ONNRPVYIPRPRPPHPRL-NH₂). In their deprotonated states, the C-terminus of Api88 is negatively charged (COO⁻) and the one of Api137 neutral (CONH).

Our collaborators found that Api88 binds to the exit tunnel in a position similar to that of Api137 (Figure 2.3). Still, the cryo-EM density is less defined, necessitating the usage of multiple conformations to model it. The density showed that Api88 could take a downward (conformation I) or upward (conformation II) conformation near its Arg17 residue. Further, the density protrudes towards the PTC, which could only be explained by conformation III. The latter model is shifted by 3.2 Å compared to the other conformations.

2.4. Cryogenic electron microscopy

The following section is based on Milne et al. [17], if not specified otherwise.

Cryogenic electron microscopy (cryo-EM) is a type of transmission electron microscopy that is used to study biological macromolecules under cryogenic conditions. It has evolved as one of the leading imaging methods for the structure determination of biological macromolecules, along with X-ray crystallography and nuclear magnetic resonance spectroscopy [17]. Transmission electron microscopy exploits Abbe's law, stating that the resolution of a microscope is inversely proportional to the wavelength of the illumination source by using electrons as an illumination source. The De-Broglie wavelength of electrons is much shorter than that of electromagnetic waves in the visible spectrum, leading to higher resolution in transmission electron microscopes than con-

2. Background

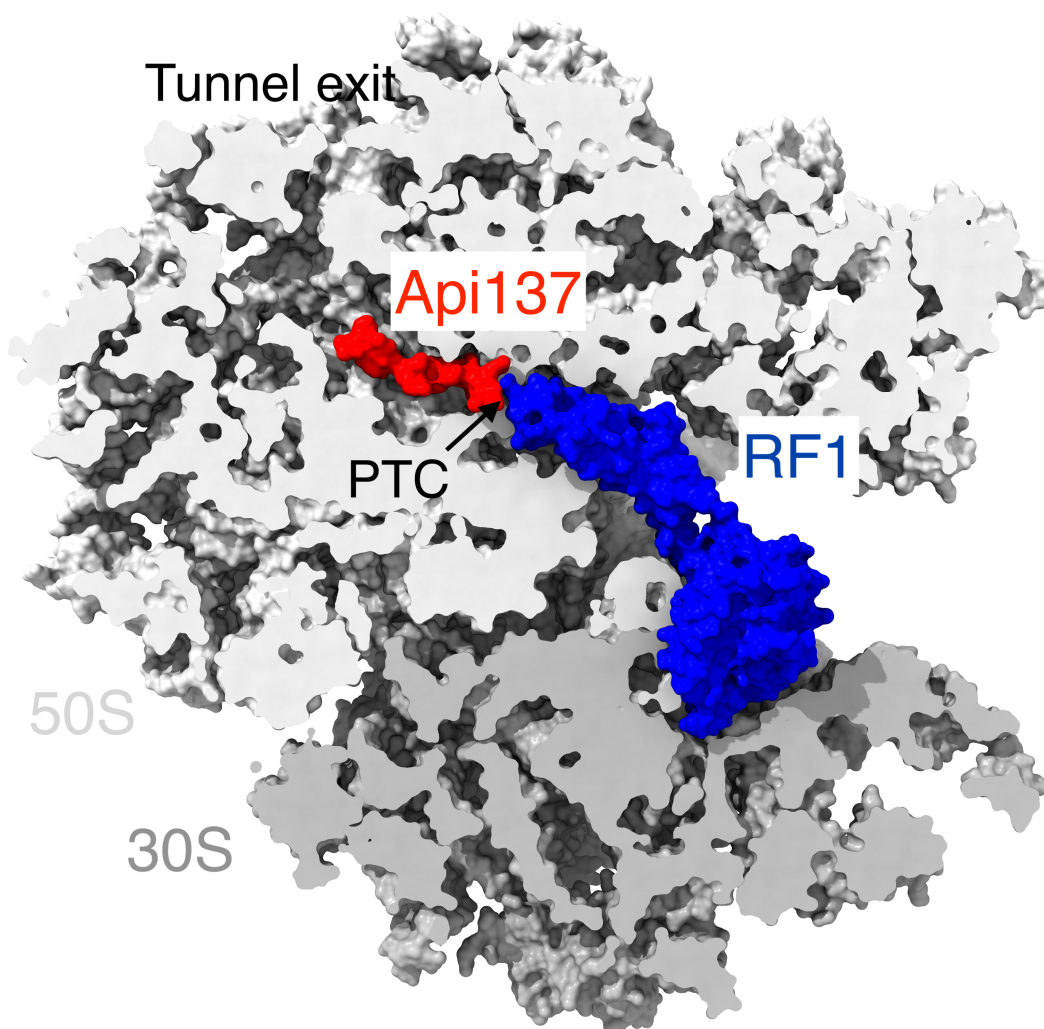


Figure 2.2.: Api137 (red) bound to a release factor (blue) at the ribosomal A site. A cross-section of the surrounding 70S ribosome is depicted in the background (grey). The ribosome model was taken from Florin et al. [7] (PDB ID 5O2R).

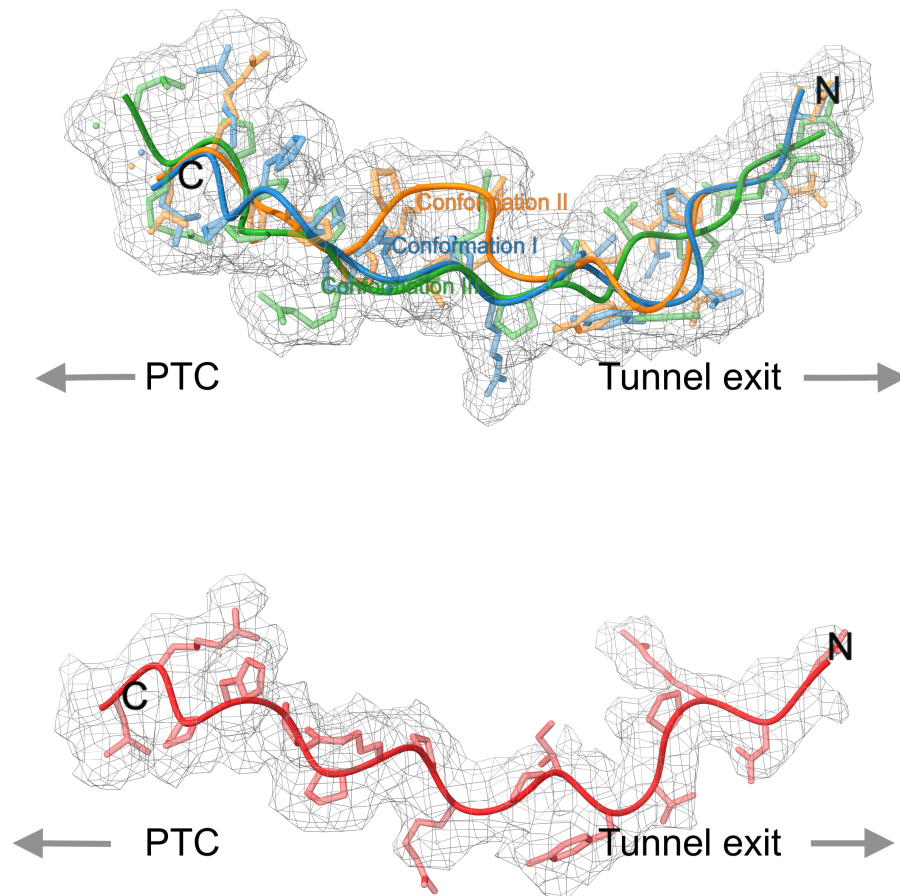


Figure 2.3.: Cryo-EM structures of Api137 and Api88. The upper panel shows three different conformations of Api88, while the lower shows a single Api137 model. The surrounding cryo-EM density is shown as a black mesh.

2. Background

ventional light microscopes. However, imaging a biological sample like a protein with a transmission electron microscope at room temperature would be difficult because the electron dose needed for a sufficient signal-to-noise ratio would inflict massive radiation damage on the sample. Cryo-EM microscopists overcome this obstacle by shock-freezing (*vitrifying*) the sample in liquid nitrogen or liquid helium before imaging, because low temperatures drastically decrease the amount of radiation damage inflicted upon the sample. A fast cool-down of the sample prevents the formation of ice crystals and ensures the sample retains a near-native state.

Single-particle cryo-EM is used to obtain structures of individual macromolecules. The workflow starts with spreading a solution of sample molecules on a carbon grid, where the samples are ideally spread evenly in a variety of orientations. After that, the sample is vitrified. From the resulting 2-dimensional micrographs of the randomly oriented particles, a 3-dimensional electron density map can be calculated with specialised software tools, e. g. *SPIDER* [18] or *IMAGIC* [19]. After further refinement of the map, an atomic model is fitted to it with software tools like *ChimeraX* [20] or *Coot* [21].

The resolution of a 3D reconstruction is measured by the Fourier shell correlation (FSC). The FSC is a measure of cross-correlation as a function of spatial frequencies between independent 3D reconstructions in Fourier space, each computed from half of the 2D micrographs. The map resolution is determined at a specific FSC cutoff-value (normally 0.143) [22].

2.5. Molecular dynamics simulations

2.5.1. The MD algorithm

MD simulations are a computational method for studying the dynamics of atomic systems based on numerically solving Newton's equations of motion. They forego a computationally expensive quantum mechanical approach that relies on directly solving the time-dependent Schrödinger equation

$$i\hbar\partial_t\Psi = H\Psi. \tag{2.1}$$

Instead, molecular dynamics uses well-motivated approximations and semiempirical force fields to achieve experimentally verifiable results. A comprehensive overview of the MD algorithm can be found in Berendsen et al. [23]. The first step to simplify the description of motions a system of atoms performs is to apply the Born-Oppenheimer approxima-

tion. It is based on the observation that electrons move much faster than their corresponding nuclei, making it possible to separate the atomic wave function Ψ into an electronic and a nucleic part: $\Psi = \psi_n \psi_e$. The second approximation is the treatment of the nuclei as point particles that follow Newtonian equations of motion, which are solved via a leap-frog Verlet algorithm

$$\vec{v}_i \left(t + \frac{\Delta t}{2} \right) = \vec{a}_i(t) + \vec{v}_i \left(t - \frac{\Delta t}{2} \right) \quad (2.2)$$

$$m\vec{a}_i(t) = -\nabla V(\vec{R}_i(t)). \quad (2.3)$$

The effect of electrons, which are assumed to be in their quantum mechanical ground state, on the dynamics of the nuclei is approximated as a potential energy surface. Equation 2.2 represents the velocity update step of an atom i at position \vec{R}_i from the velocity of the previous time step. The force acting on that atom is calculated from the force field V (Equation 2.3).

The forces that govern the nucleic motion can be approximated as a sum of bonded interactions with a purely quantum mechanical origin and non-bonded interactions with an electrostatic or hybrid origin. Bonded forces describe the covalent interactions between atoms. Their associated potential

$$V_{\text{bonded}} = V_{\text{bond}} + V_{\text{angle}} + V_{\text{dihedral}} \quad (2.4)$$

consists of contributions from bond lengths, bond angles and dihedral angles. The non-bonded forces describe the electrostatic and van-der-Waals (vdW) interactions:

$$V_{\text{nonbonded}} = V_{\text{electrostatic}} + V_{\text{vdW}}. \quad (2.5)$$

Hydrogen bonds are treated as purely electrostatic for computational simplicity, although they have a quantum-mechanical contribution. All of these energy terms can be expressed as a specific functional form, e.g. a harmonic, Lennard-Jones, or Coulomb potential, with particular parameters. A collection of functional forms and parameters makes up a force field, which serves as computationally simplified approximation of the true quantum-mechanical forces. Parameter values are often inferred from experiments but can also be computed *ab initio* from quantum-chemical simulations of individual molecules. Many different force fields are available and users must carefully examine their system and choose the force field that fits their needs. Some of the most commonly used include GROMOS [24], AMBER [25], CHARMM [26] and OPLC [27].

2.5.2. Solvent treatment

As biomolecules do not exist in a vacuum, the solvent must also be considered in MD simulations. For many MD simulations of biomolecules under physiological conditions, the solvent will mainly consist of water molecules interspersed with a few ions to reproduce physiological salt concentrations and neutralise the system's net charge. There are different options to simulate water molecules. The most straightforward method represents the oxygen and hydrogen atoms with a point charge, resulting in a three-point water model, e. g. TIP3P [28]. To save computational costs, two-point models are available that aim to approximate the electrostatic charge field of the whole water molecule rather than represent each atom [29]. Four-point or higher-order models are also used in many circumstances because the additional point charges provide a more accurate representation of the molecule's charge distribution [30]. Of course, there cannot be infinite solvent molecules, so the simulation system must be finite in size. All solute and solvent atoms are placed in a three-dimensional box, whose specific shape depends on many factors. Cubic or dodecahedral box shapes are often used. MD simulations normally are performed under periodic boundary conditions, where the box size has to be chosen large enough so that the solute is not influenced by its periodic image.

2.5.3. Calculation of long-range electrostatic interactions

Generally, most of the available computational power in an MD simulation is spent computing nonbonded electrostatic interactions. These pose computationally intensive problems, as they are long-ranged and undirected. The computational effort scales proportional to the square of atoms in the system ($\mathcal{O}(n^2)$). Thus, it is required to compute the interactions of each atom with every other atom. *Particle Mesh Ewald* provides an algorithm significantly reducing computational effort to $\mathcal{O}(n \log n)$ [31]. The underlying theory of Ewald summation states that the electrostatic interactions can be split into short-ranged and long-ranged contributions, the latter of which can be evaluated in Fourier space. This trick allows the long-range part calculation to converge more rapidly than it would in real space.

2.5.4. Temperature and pressure coupling

A simulation conducted as described above would always keep the sum of kinetic and potential energy constant, representing a microcanonical (NVE) ensemble. This does not represent realistic experimental conditions, where a sample constantly exchanges

energy with its surroundings. Therefore, it is important to couple the simulation system to virtual heat (thermostat) and pressure (barostat) baths to obtain canonical (NVT) or isothermal-isobaric (NPT) thermodynamic ensembles. There are various ways to implement thermostats and barostats. Two common options implemented in the *GROMACS* simulation software [32] are described here:

The v-rescale thermostat

The stochastic velocity rescaling thermostat (v-rescale) [33] was introduced to sample a correct NVT ensemble while allowing for fast equilibration of the system to a target temperature with the corresponding average kinetic energy \bar{K} . At every integration step dt the total kinetic energy K is updated by

$$dK = (\bar{K} - K) \frac{dt}{\tau} + \sqrt{\frac{2K}{\beta\tau}} dW \quad (2.6)$$

and the kinetic energies of the particles are rescaled to enforce this value. The first term is a relaxation of the system towards the target temperature with the time scale τ . The second term adds a stochastic fluctuation in the form of a Wiener process dW . β refers to the inverse target temperature.

The c-rescale barostat

The stochastic cell rescaling barostat (c-rescale) [34] relies on a similar idea as the v-rescale thermostat. Its application leads to the correct sampling of the NPT ensemble. At each integration time step, the strain

$$\epsilon = \ln \frac{V}{V_0} \quad (2.7)$$

is updated. V_0 refers to a reference volume and V to the volume of the simulation box at the current time. The update step takes the form

$$d\epsilon = -\frac{\beta_T}{\tau_P} (P_0 - P) dt + \sqrt{\frac{2k_B T \beta_T}{V \tau_P}} dW. \quad (2.8)$$

P_0 refers to the external pressure of the barostat, P to the system's internal pressure, β_T to the isothermal compressibility of the system and τ_P is the time scale of the pressure coupling.

2.6. Principal component analysis

Molecular dynamics trajectories exhibit diverse fast and slow, small- and large-scale motions. It can be difficult to identify the functionally relevant conformational changes in an MD trajectory. Principal component analysis (PCA) can greatly reduce the dimensionality of a given trajectory's configurational space by defining a new basis set in configurational space. The axes are chosen to maximise the variance of the trajectory projections onto the axes. Those projections then show collective motions with the largest fluctuations, which we assume to be also the functionally most significant ones.

The following section is based on a review of principal component analysis by Palma and Pierdominici-Sottile [35].

In Cartesian space, a snapshot of a system of N atoms is represented by $N3$ -dimensional vectors, while in configurational space it can be written as a single $3N$ -dimensional vector. The whole trajectory is thus a set of M snapshots $\{\vec{x}^{(k)}\}$, with k running from 1 to M . The following steps are applied for PCA.

1. Remove translational and rotational motions by rigid-body-fitting all snapshots to a reference structure.
2. Calculate the covariance matrix

$$C_{ij} = \frac{1}{M} \sum_{k=1}^M (x_i^{(k)} - \langle x_i \rangle) (x_j^{(k)} - \langle x_j \rangle). \quad (2.9)$$

$\langle x_i \rangle$ and $\langle x_j \rangle$ represent the average values of all snapshots for the i th and j th coordinates respectively.

3. Diagonalise the covariance matrix by solving the eigenvalue equation

$$C\vec{v}_n = \lambda_n \vec{v}_n \quad (2.10)$$

The eigenvectors $\{\vec{v}_n\}$ form a new orthogonal basis set. The eigenvalues corresponding to the eigenvectors are the variance of the respective trajectory projections. When sorted by the magnitude of corresponding eigenvalues in decreasing order, the first eigenvector is oriented to maximise the variance of the data projected onto it. The second eigenvector has the same property under the additional condition of being orthogonal to the first.

4. Project the trajectory onto the subspace spanned by one or more eigenvectors.

A projection onto the subspace spanned by e. g. the first two eigenvectors shows the simulated molecule’s movement along the two most essential axes of motion.

When the simulation has not converged to equilibrium yet, it is possible that random diffusion resembles large-scale collective motion and is therefore described by the first few eigenvectors. In order to not mistake eigenvectors that describe random diffusion for functionally relevant motions, the cosine content of the respective eigenvectors should be examined. A high cosine content of the projection onto the corresponding eigenvector signifies a high similarity to random diffusion [36].

2.7. Computation of density maps from atomic models

To compare molecular dynamics data to an experimental density map, it is useful to calculate a density map via Gaussian spreading from snapshots of molecular dynamics trajectories [37]. From each atom, an isotropic point spread function is derived. It takes the form of a superposition of N_G Gaussians. At distance d , the density is

$$P(d) = \sum_{i=1}^{N_G} A_i e^{-B_i d^2}. \quad (2.11)$$

A_i and B_i are coefficients derived from the specific atom type’s scattering factors. These differ depending on the experimental scattering method used for the reference map (X-ray scattering or cryo-EM). The software GROmaps, which is used here for density map calculation, has tabulated values of the coefficients for X-ray crystallography and cryo-EM [37]. The total density distribution ρ of all N atoms in the system is calculated as a superposition of the individual atoms’ contributions. It is evaluated on a discrete 3-dimensional lattice with M lattice points $\{\vec{g}_j | j = 1, \dots, M\}$:

$$\rho(\vec{g}_j) = \sum_{i=1}^N P(\|\vec{g}_j - \vec{R}_i\|) \quad (2.12)$$

\vec{R}_i represents the position of the i th atom.

2.8. Root mean square deviation

The root mean square deviation (RMSD) is an observable that can be used to compare the structural similarity of two models or investigate the deviation of a trajectory from

2. Background

its initial structure as a function of time [38]. Before calculating the RMSD, all involved structures should be rigid-body fitted to a reference structure. Otherwise, a translation or rotation of the whole model might skew results, because it would lead to a large RMSD without the internal model structure being necessarily different from the reference model. Assuming we want to compare a structure with N atoms taken from an MD trajectory at time t_2 with the simulation's initial structure at time t_1 , the mass-weighted RMSD is calculated as follows:

$$\text{RMSD}(t_1, t_2) = \sqrt{\frac{1}{M} \sum_{i=1}^N m_i |\vec{r}_i(t_2) - \vec{r}_i(t_1)|^2} \quad (2.13)$$

\vec{r}_i is the position of atom i and m_i its mass. $M = \sum_{i=1}^N m_i$ denotes the total mass. The RMSD is often consulted as a convergence indicator when plotted as a function of simulation time. For a fully equilibrated simulation, it is necessary for the RMSD to not show a continuous upward-trend anymore. However, a flat RMSD-over-time function is not a sufficient criterion to prove that a simulation with finite length has reached equilibrium.

2.9. Root mean square fluctuation

The root mean square fluctuation (RMSF) measures the fluctuation of an atom i around its mean position $\langle \vec{r}_i \rangle$, i. e. it represents the standard deviation of the atom position \vec{r}_i [39]:

$$\text{RMSF}_i = \sqrt{\langle |\vec{r}_i - \langle \vec{r}_i \rangle|^2 \rangle} \quad (2.14)$$

In contrast to the RMSD the RMSF does not highlight the deviation of a structure from its initial coordinates over the course of a simulation but measures a molecule's flexibility. Regions with high RMSF values show high structural flexibility, while regions with low RMSF values are more rigid.

2.10. Pearson correlation coefficient

The Pearson correlation coefficient is a statistical measure to calculate the linear correlation between two data sets [40]. Given data X and data Y , their correlation is defined

as the covariance of X and Y divided by their respective standard deviations:

$$\rho = \frac{\langle (X - \langle X \rangle)(Y - \langle Y \rangle) \rangle}{\sqrt{\langle (X - \langle X \rangle)^2 \rangle} \sqrt{\langle (Y - \langle Y \rangle)^2 \rangle}} \quad (2.15)$$

In the context of this thesis, it is be used to determine the correlation of two electron-density maps.

2.11. Bootstrapping

Bootstrapping is a method of inferring the statistics of a population from a sample of that population via resampling [41]. In many situations, only a small sample of an unknown underlying population is known. Thus, the statistical properties of the sample will differ with a certain unknown error from those computed from the population. In this case, N resamples of the original sample can be produced via sampling with replacement. From the resamples, a distribution of the desired statistic can be calculated. If the sample is representative of the population and N was chosen sufficiently large (normally on the order of magnitude of 1000 or 10 000 resamples), this distribution will asymptotically approach one obtained from resampling the true population N times.

3. Methods

3.1. Simulation Setup

3.1.1. System preparation and energy minimisation

Our collaborators from the group of Christian Spahn (Charité Berlin) provided us with four structure models based on cryo-EM maps of 50S-Api complexes, one for Api137 and three for the different conformations of Api88. To isolate the influence of the C-terminus, I created an additional structure from the Api137 structure, where I kept all atomic coordinates but changed the C-terminal acid into an amide. This resulted in a structure which chemically corresponds to Api88 and has the conformation of Api137 and will be referred to as Api137-NH₂. I then carried out simulations starting from five structures: conformations I, II, and III of Api88 as well as Api137 and Api137-NH₂. To obtain an extensive sampling of the conformational space and to be able to calculate uncertainties of the results, I ran 15 independent replica simulations from each of these five initial structures of Api88/137 in the ribosomal exit tunnel for a duration of 2 μ s.

Since in the cryo-EM structures the 50S subunit is unchanged, with the exception of the tunnel residues in contact with the antimicrobial peptide, I simulated a cut-out volume centred around the peptide, thereby reducing the computational effort. To that aim, all residues located within 3.5 nm around the Api peptide were included in the simulation system. Due to the hard cutoff distance, some RNAs or proteins were broken, because a single or more nucleotide or amino acid residues lay outside the cutoff distance and was not included in the cutout volume. When only a single residue was outside the 3.5 nm radius, but its 5'- and 3'- (n- and c-) neighbours were inside, the residue was included in the simulation volume. When more than one consecutive residue in a nucleotide or peptide chain were outside the radius, the nearest neighbours inside the radius were treated as terminal residues. All peptide chains (except Api) were capped by an N-terminal acetyl and a C-terminal amide. Subsequently, I used WHATIF [42] to determine the protonation states of histidine residues. Missing hydrogen atoms were

3. Methods

added with *gmx pdb2gmx*.

As the cryo-EM structures did not contain structural ions and water molecules, I added them from another previously resolved 50S subunit structure. To that aim, I superimposed the structure of an *E. coli* (PDB id: 6PJ6) [43] 50S subunit on the five 50S-Api structures and copied the ions and water molecules in the 3.5 nm cutout volume and 0.5 nm distance to the atoms of the 50S-Api structure.

Then, I placed each structure in a dodecahedral simulation box with a distance of at least 1.5 nm between the outer atoms and the box boundaries.

Next, the simulation box was solvated with water molecules and ions. I recreated a physiological salt concentrations of 3.5 mmol L⁻¹ for MgCl and 150 mmol L⁻¹ for KCl and then neutralised the total system charge with K⁺ ions by using the GROMACS programmes *gmx solvate* and *gmx genion* [32]. I used the K⁺ and Cl⁻ ion parameters from Joung and Cheatham [44] and the microMg parameters from Grotz and Schwierz [45]. Amber14sb [25] was chosen as a force field, and OPC3 [46] as a water model.

To increase the simulation time step from 2 fs to 4 fs, the hydrogen atoms were described as virtual sites, adding their masses to the heavy atoms they were linked to. Their positions during the simulations were then calculated geometrically. The virtual sites represent the centre of mass of all hydrogen atoms linked to the same heavy atom. The centre of mass moves much slower than the actual hydrogen atoms, allowing for a larger integration time step. All simulations were conducted with the GROMACS 2023 simulation suite [47].

The solvated structure was used as input to a potential-energy minimisation that moved solvent atoms into positions where their energy corresponded to a local minimum. This step is crucial because otherwise, an MD simulation might become numerically unstable due to large initial forces. The energy was minimised for 6000 steps using a steepest-descent algorithm with an initial step size of 0.01 nm for the atom positions. The potential energy was regarded as converged to a local minimum when the maximum force was smaller than 10 kJ mol⁻¹ nm⁻¹. Solute atoms (including structural water molecules and ions) were kept in place with position restraints to maintain the experimentally determined structure. Position restraints are additional harmonic potentials (here with a spring constant of 1000 kJ mol⁻¹ Å⁻²) centred on the initial positions of the atoms and energetically punish movement of the restrained atom.

3.1.2. Solvent equilibration

The system had to be adequately equilibrated before gathering any data from the simulation. The equilibration MD simulation started from the atomic coordinates of the energy-minimised structure and initial velocities were drawn from a Boltzmann distribution at a temperature of 300 K. The solute atoms were held in place with the above-described position restraints, and the solvent was equilibrated for 50 ns in the NPT ensemble. The temperature was set to 300 K and the pressure to 1 bar. I used the *v-rescale* thermostat for temperature coupling and the *c-rescale* barostat for pressure coupling.

3.1.3. Release of position restraints

All solute atoms were held in place with position restraints for the solvent equilibration. In the production simulations these had to be released with the exception of the outer layer of the simulation system: Due to the simulation system being a cutout of a whole 50S subunit, the atoms at the surface of the cutout volume missed interactions with removed ribosome atoms, which would have led to the simulation volume falling apart [11]. The effect of these interactions were mimicked by applying position restraints to the outer atoms of the simulation volume that allow a similar movement range as they would have in the intact 50S subunit [48].

The restraints were applied to all atoms positioned at a distance of 25 Å to 35 Å (outer layer) from the Api peptide. The spring constants of the outer layer position restraints were calculated from a previously conducted simulation of an intact 70S ribosome [49]. First, a custom Python [50] script compared atoms in the outer layer of the simulation system and the reference 70S ribosome structure. If atoms in the outer layer of the apidaecin-50S structure were also present in the 70S reference, the spring constants were calculated from the root-mean-square fluctuations of the corresponding atoms in the reference simulation [48]. Otherwise, they were assigned a default spring constant equivalent to the average of all other spring constants. Over the course of a 20 ns simulation started from the equilibrated system, the position restraints were linearly decreased to the calculated values for the outer layer and to zero for the remaining atoms. After that, a production simulation of 2 μ s was started and only these trajectories were used for the following analyses.

3.2. Post-processing of simulation trajectories

Due to the periodic boundary conditions, molecules appeared broken once they partially crossed the simulation box boundary on one side and reentered on the other. These artefacts had to be removed prior to analysis. The GROMACS tool *gmx trjconv* was used for that purpose. I used it to return atoms to their original position once they crossed box boundaries.

I had to realign the simulation trajectories to their respective cryo-EM models because the system preparation introduced a translation of the whole system. I used PyMOL [51] to align the simulation input structures to the unmodified cryo-EM structures and *gmx trjconv* to align the simulation trajectories to the respective input structures via a least-squares-fitting of rRNA phosphate-atoms.

3.3. Principal component analysis

To examine the conformational changes of Api88, Api137 and Api137-NH2, I performed principal component analysis. I did not calculate a covariance matrix for each trajectory individually but rather one for all Api88 trajectories, one for all Api137 trajectories and one for all trajectories combined. For calculating the covariance over multiple trajectories with different initial structures, I had to ensure that all trajectories contained the same number of atoms. I used a custom Python script to extract all phosphate atoms that were present in all starting structures (Api88 conformations I-III, Api137 and Api137-NH2) and the heavy atoms of the Api peptides. After aligning the trajectory snapshots with a least-squares-fit of the phosphate atoms, the covariance matrix of the heavy apidaecin atoms was calculated with *gmx covar* from the combination of all Api88 (Api137 and Api137-NH2, all) trajectories, sampled at 1 frame s^{-1} . I used *gmx anaeig* to project each ensemble of trajectories associated with the same starting conformation onto the first two principal components of all Api88 (Api137 and Api137-NH2, all) trajectories. Then, I calculated a two-dimensional probability density from the projections on each unique pair of principal components up until the third component (associated with the third-highest eigenvalue).

3.4. Calculating cryo-EM maps from MD snapshots

In order to compare the MD trajectories to the cryo-EM density, I used *GROmaps* [37], a tool that calculates density maps from atomic models. In a preparatory step, I reduced the cryo-EM map to a box that included the density up until 5 Å around the three Api88 models. The new map was calculated on the same grid points as the reduced cryo-EM map using only the heavy Api atoms. Ensembles of MD trajectory originating from the same structure were represented in a single map by calculating a map for every trajectory snapshot and then averaging the density over all snapshots.

I chose the atom spread width σ to produce a map resembling the experimental density as close as possible. To that end, I calculated multiple maps of the whole 50S subunit model with σ ranging from 0.05 nm to 0.3 nm in steps of 0.01 nm. Then I calculated the Pearson correlation coefficient between each calculated 50S map and the cryo-EM map. The largest correlation could be achieved with $\sigma = 0.11$ nm.

3.5. Quantifying the contributions of Api88 conformations to the cryo-EM density

The cryo-EM density represents an ensemble of multiple conformational states of Api88, which occurred with certain frequencies in the microscopy sample. One of my research aims was to quantify the contributions (i. e. probability of occurrence) of the conformations I to III to the density. For this reason I calculated a density map for each conformation (Section 3.4) and combined them into a single map with a weighted linear combination

$$\text{Map}_{WLC} = w_1 \text{Map}_I + w_2 \text{Map}_{II} + w_3 \text{Map}_{III}. \quad (3.1)$$

The normalised weights represent the contributions of conformations I-III to the cryo-EM density. To determine their values, I treated them as optimisation variables in the context of maximising the Pearson correlation coefficient between the calculated map and the cryo-EM map. I used *scipy* [52] to solve this local optimisation problem for the weights w_1, w_2 , and w_3 under the constraint that they are normalised ($w_1 + w_2 + w_3 = 1$).

3.6. Finding optimal MD structures

The MD simulations generated a large number of snapshots of Api88 in different conformations. I wanted to find out if a combination of N snapshots might describe the cryo-EM density better than the initially modelled conformations I-III. For that purpose, I designed an algorithm that searches a large pool of MD snapshots from Api88 simulations for a set of N structures that provide an optimal description of the cryo-EM density. The likeliness to the cryo-EM map is quantified by the correlation coefficient between the cryo-EM map and a weighted linear combination of maps calculated from the N structures.

The search started with an initial set of N structures and iteratively exchanges structures to increase the correlation. First, I extracted a frame every 250 ns from each of the 75 Api88 trajectories and calculated the respective density map of each of these frames. These make up the pool of structures to choose from. After that, I picked a set of N maps from the pool at random, with N being a fixed integer. Using these maps, I constructed a new map as a weighted linear combination that maximises correlation to the cryo-EM map. The set of maps was edited iteratively to increase the correlation to the cryo-EM map. Each iteration consisted of the following two steps:

1. Randomly pick one of the N selected maps and exchange it for another map picked randomly from the pool.
2. Construct the correlation-optimising weighted linear combination.

If the correlation exceeded the result of the previous iteration, the updated set of structures was used as input for the next iteration. Otherwise, it was discarded.

The above procedure was performed for several set sizes N separately. For quicker sampling, five independent searches were started for each N . Each search continued until 5000 iterations had passed. Inspections of the final correlation coefficients from each run showed disagreement no larger than 1×10^{-3} between the search runs for a fixed N .

4. Results and discussion

4.1. Principal component analysis of Api88 trajectories

One of the research questions I wanted to address was finding out if the Api88 conformations quickly interconvert or represent metastable states for an extended time period. This question can hardly be answered by simply looking at the trajectories. PCA provides a way to easily visualise which areas in conformational space are occupied by which trajectories. When performed in cartesian space, the principal components correspond to conformational changes of the analysed molecules, therefore I will refer to them as conformational modes.

I performed PCA on all Api88 trajectories together (see section 3.3). The first mode represents a shift of the peptide towards or away from the PTC, while the second displays mainly a disposition of the N-terminal residues (Figure 4.1). They have eigenvalues of $\lambda_1 = 11.58 \text{ nm}^2$ and $\lambda_2 = 4.16 \text{ nm}^2$ respectively. Together, the first two conformational modes account for 48.73 % of the variance in the Api88 trajectory data.

Figure 4.1 shows a clear separation between the projections of conformation-III-based trajectories and the trajectories started from conformations I and II. No trajectories originating from conformation III cross over to the area occupied by simulations of conformation I and II. Trajectories starting from conformation III occupy the lower values of the first conformational mode and the other two conformations occupy the higher values.

The separation of conformation III and conformations I and II projections on the first conformational mode highlights that the former does not interconvert into the other two and keeps its C-terminal protrusion towards the PTC. The projection does not show a distinction between conformations II and III.

The result suggests that conformation III represents a metastable state at least on the time scale of $2 \mu\text{s}$. Apparently, the deeper protrusion towards the PTC is associated with a high energy barrier, that is only overcome on larger time scales.

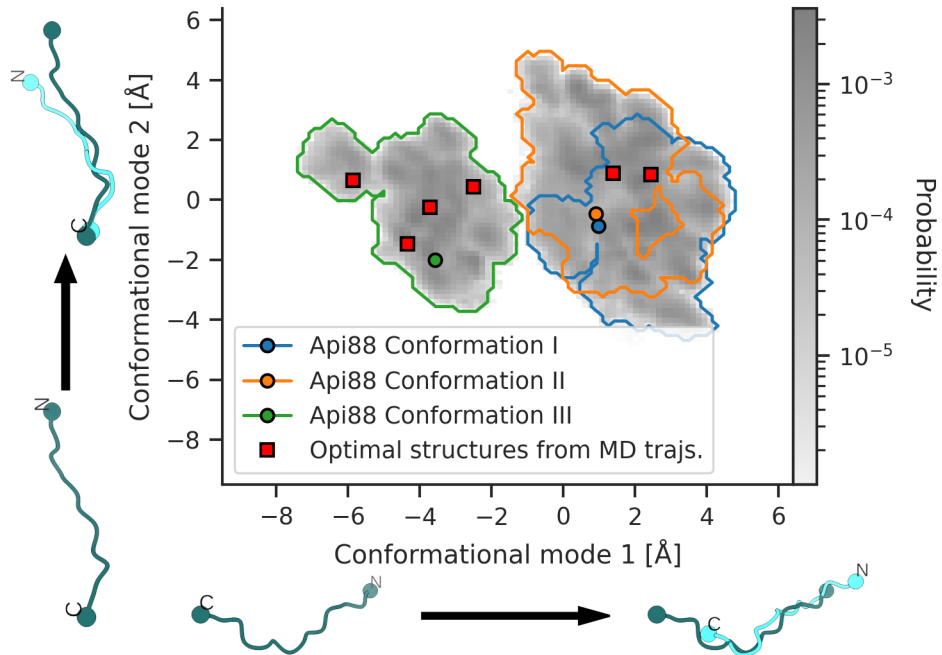


Figure 4.1.: 2D projection of Api88 trajectories onto the first two principal components (conformational modes). Grey values indicate the sampling probability of the corresponding point in conformational space. Coloured contours encompass trajectories starting from the same conformation. Circles of the same colour denote projections of the respective starting conformations. Red squares represent a set of six structures from the Api88 MD trajectories that give an optimal explanation of the cryo-EM map (described in section 4.3). Extreme conformations along each principal component are displayed as dark and bright turquoise renderings below the x- and left of the y-axis.

4.2. Contributions of Api88 conformations to the cryo-EM density

Next, I aimed to use the MD simulation data to quantify the contributions of the modelled Api88 conformations I-III to the cryo-EM density map. To that end, I calculated density maps from the Api88 conformations and combined them with weights that maximise the correlation to the resulting map to the cryo-EM map (see Sections 3.4 and 3.5). With optimal weighting, a correlation coefficient of 0.375 can be achieved. Conformation III contributes the most to the calculated map with a weight of 0.46. The conformations I and II have smaller, but still considerable weights ($w_1 = 0.22$, $w_2 = 0.33$).

Subsequently, I examined if the inclusion of more conformations increases the correlation to the cryo-EM map. Therefore, I expanded the map calculation from only the initial conformations to the MD trajectories originating from them. For all trajectories starting from the same conformation, I calculated an average density map, now representing the density of a conformational ensemble. The correlation coefficients between the cryo-EM map and a variety of possible combinations of ensemble maps is shown in Figure 4.3a. The maximum correlation coefficient is 0.414. The corresponding optimal weights are 0.63 for conformation III, 0.26 for conformation II and 0.11 for conformation I.

The increase of the correlation coefficient from the initial structure to the MD ensemble gives rise to the question if the correlation is actually stabilised after 2 ns. To assess how the correlation evolves as a function of simulation time, I calculated optimised correlation coefficients from the ensembles of shortened partial trajectories with lengths of 1 ns, 5 ns, 10 ns, 50 ns, 100 ns, 500 ns and 1000 ns. Figure 4.2 shows how the correlation coefficient quickly increases after a short simulation time. It rapidly reaches values in the vicinity of the 2 μ s-average and does not increase significantly anymore after about 100 ns. It cannot be ruled out that the correlation would start to increase again in an even longer trajectory, but this would then be caused by a large conformational change. For the consideration of a conformational ensemble that remains close to the initial conformations, 2 μ s is a sufficient simulation time to capture a stable ensemble correlation.

In summary, the weights obtained for the initial structures and the weights obtained from the MD ensembles show that conformation III contributes most to the cryo-EM density and seemingly is the most frequent binding mode of Api88 in the exit tunnel. This effect is more pronounced when the MD ensemble is considered, highlighting the importance of taking additional conformations into account when describing the cryo-EM

4. Results and discussion

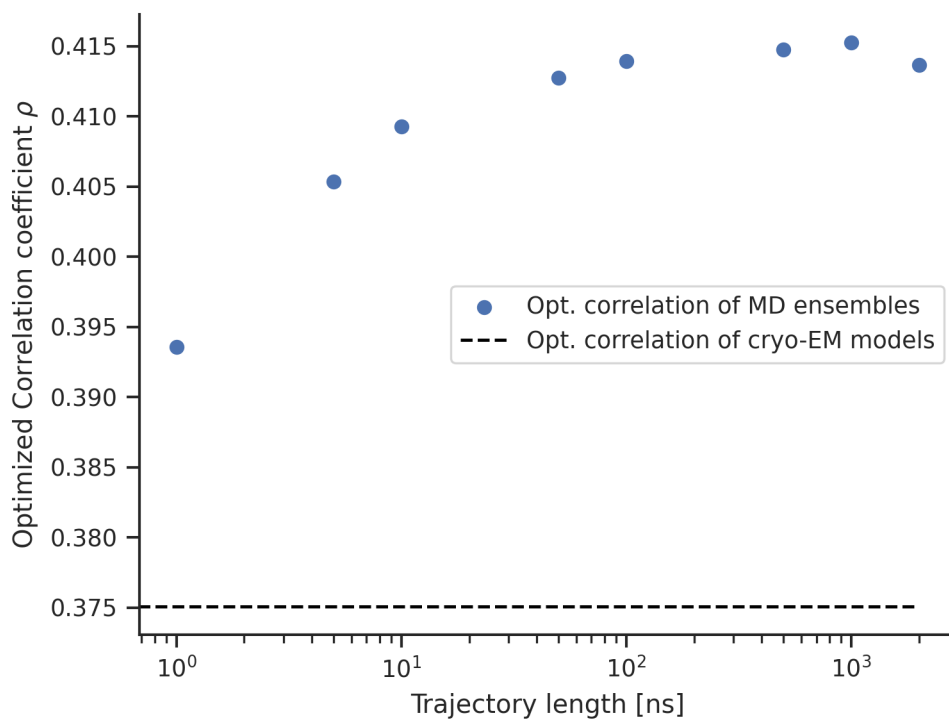


Figure 4.2.: Cumulative correlation over simulation time. A density map was calculated for each partial trajectory up until times $t = 1$ ns, 5 ns, 10 ns, 50 ns, 100 ns, 500 ns, 1000 ns and 2000 ns. Then, the maps were averaged over all replicas. Finally, the maps from all three simulation ensembles were combined in a weighted linear combination that optimises the correlation to the cryo-EM density at each point in time. The dashed black line represents the correlation of the optimally weighted combination map of the initial structures to the cryo-EM density.

density. Here, the conformation-III ensemble contributes more than half of the density to the calculated map that fits the cryo-EM density best.

4.3. Improving explanation of cryo-EM data with MD-generated conformations

Another aim of this study was to identify MD structures that might describe the cryo-EM density equally as good or better as the initial three models. In the previous section, I showed that the MD ensembles started from conformations I-III achieve a better explanation of the cryo-EM density than the models themselves. In this section, I aim to find a small set of specific structures from the MD trajectories that have an improved correlation to the cryo-EM map.

For that purpose, I designed an algorithm that repeatedly picks structures from the Api88 MD trajectories, calculates their corresponding density maps, and finds an optimally weighted linear combination that maximises the correlation of the combined map with the cryo-EM map for the given set of structures (section 3.6).

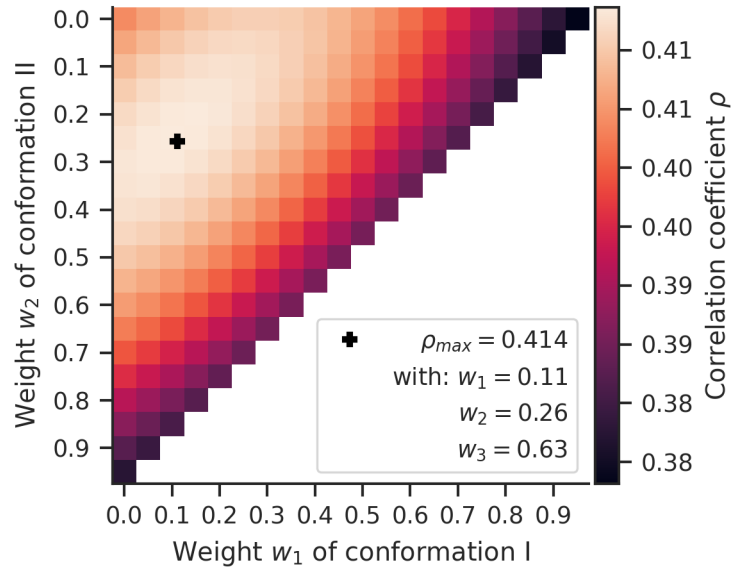
I found a set of six structures (Figure 4.4) to achieve a higher correlation than the MD ensembles (Figure 4.5). Their optimised weights are uniform. The correlation coefficient would likely increase further with larger sets, but I used the ensemble correlation as a reference point to avoid over-fitting. Six structures were sufficient to achieve a correlation similar to the ensemble correlation. The projections on the principal components of the six selected structures is shown in Figure 4.1. Four of six structures were obtained from the MD trajectories based on conformation III.

In summary, the six MD structures describe the cryo-EM density better than the three initial conformations and equally as good as the MD ensembles. Four of those structures showcase a similar shift towards the PTC as in conformation III, providing more evidence that the PTC-shifted position of Api88 contributed most to the cryo-EM density.

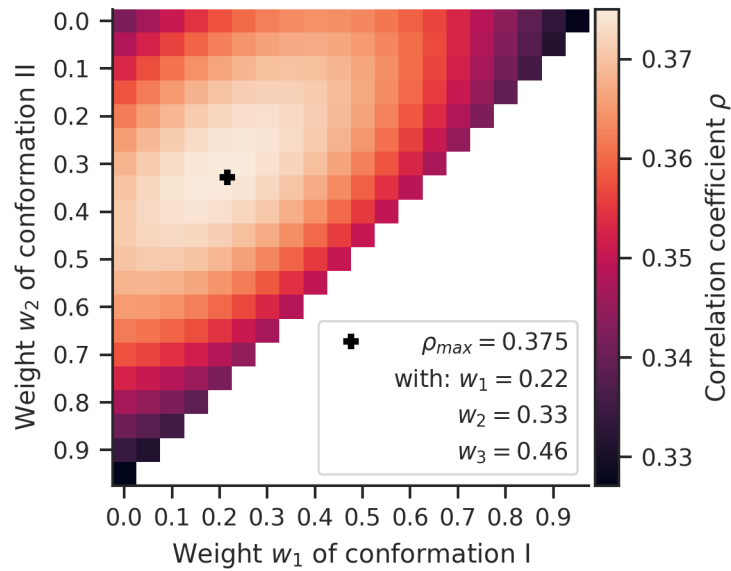
4.4. Influence of the C-terminus on binding dynamics of Api88 and Api137

The only chemical difference between Api137 and Api88 is their C-terminus. Api137 carries a carboxylic acid, COOH, which is negatively charged in deprotonated form, while Api88 carries the carboxamide CNH₂. I examined the effect of the altered C-

4. Results and discussion



(a)



(b)

Figure 4.3.: (a): Correlation coefficient between cryo-EM map and weighted linear combination of the maps computed from the MD ensembles originating from Api88 conformations I, II and III. Possible combinations of weights in steps of 0.05 are shown. The axes are labelled with the weights of conformations I and II. The weight of conformation III can be deduced from them, as they always sum to 1. The black cross signifies the maximum correlation coefficient under optimal weighting. (b): Correlation coefficient between cryo-EM map and a weighted linear combination of the maps computed from the initial Api88 conformations I, II and III. Note that the colour scale for the correlation coefficient is mapped to values different from the one in panel (a).

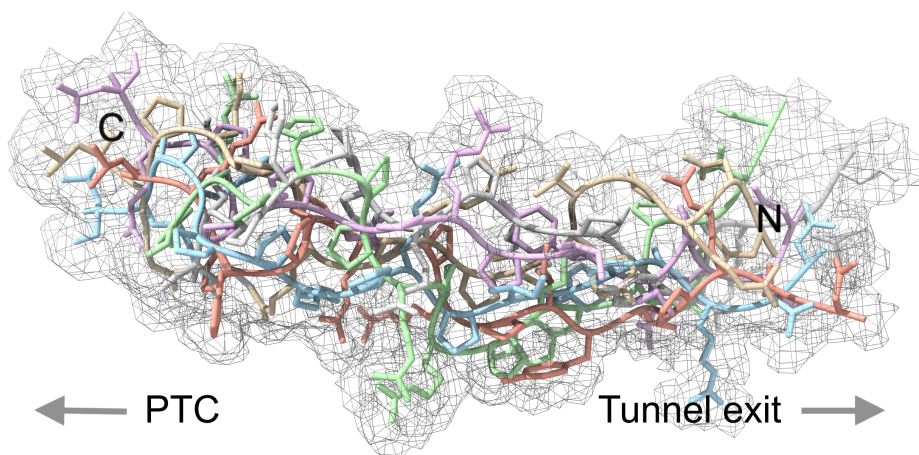


Figure 4.4.: Six snapshots from the Api88 MD trajectories. The structures were chosen to optimise the correlation coefficient between the density map calculated from snapshots and the cryo-EM map (black mesh).

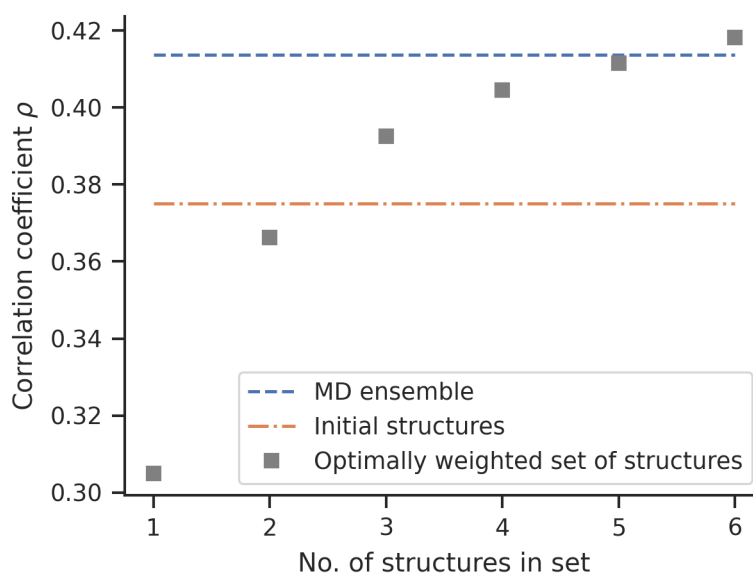


Figure 4.5.: Grey squares show the correlation coefficients between the weighted linear combination of a correlation-optimised set of structures from the MD trajectories and the cryo-EM maps. The correlation coefficient is displayed as a function of the set size. The dashed blue line and dash-dotted orange lines show the correlation coefficient for the MD ensemble and initial conformations, respectively.

4. Results and discussion

terminus on peptide dynamics by editing the cryo-EM model of Api137. To that aim, I exchanged the C-terminal acid for an amide (Api137-NH₂) and also started simulations from the resulting structure.

The root mean square deviations of the MD snapshots from their respective initial structures show differences between Api137 (Figure 4.6, red) and the amidated Api137-NH₂ (Figure 4.6, purple) as well as Api88 (Figure 4.6, left side). The RMSD time series of Api137 show less variance than in the other simulations and reach lower RMSD values overall (Figure 4.6). The RMSD time series of Api88 show now significant differences between the three conformations. RMSD analysis shows that Api137 remains more similar to its initial conformation than the other peptides. Apparently the chemical composition of the C-terminus determines whether the peptide adopts a flexible (Api88) or more conformationally stable binding mode (Api137).

Next, I studied which peptide regions contribute most to the structure deviation by computing the root mean square fluctuation for each residue. The RMSF shows decreased flexibility in Api137. This is especially noticeable in the C-terminal region, but the effect extends over the whole peptide. Further, the variance of RMSF values between replica simulations is smaller for Api137, as evidenced by the 95 % confidence intervals, which were determined via bootstrapping with 10 000 resamples.

I employed principal component analysis to highlight differing conformational modes for Api137 and Api137-NH₂. I projected the combined trajectories onto their first two conformational modes (Figure 4.8). The conformational modes represent conformational changes of the N-terminal region (mode 1) and a combination of a peptide shift along the exit tunnel and an N-terminal conformational change (mode 2). The trajectories of Api137-NH₂ occupy a larger conformational space than the trajectories of Api137. The latter also shows a more pronounced N-terminal conformation change along the first PC.

All three analyses show that Api137 possesses less flexibility than Api88 and Api137-NH₂ which is in agreement with the well-defined cryo-EM density of Api137.

It is interesting to note that the effect cannot be solely attributed to the different positioning of Api88 and Api137 in the tunnel. Api137-NH₂ shares the same starting coordinates as Api137 but still exhibits increased flexibility over the whole peptide chain. Rather, the modified C-terminus seems to change the peptide's binding behaviour. My results suggest that this effect is not restricted to the C-terminal region, but extends over the whole peptide chain, as shown by the RMSF analysis.

4.4. Influence of the C-terminus on binding dynamics of Api88 and Api137

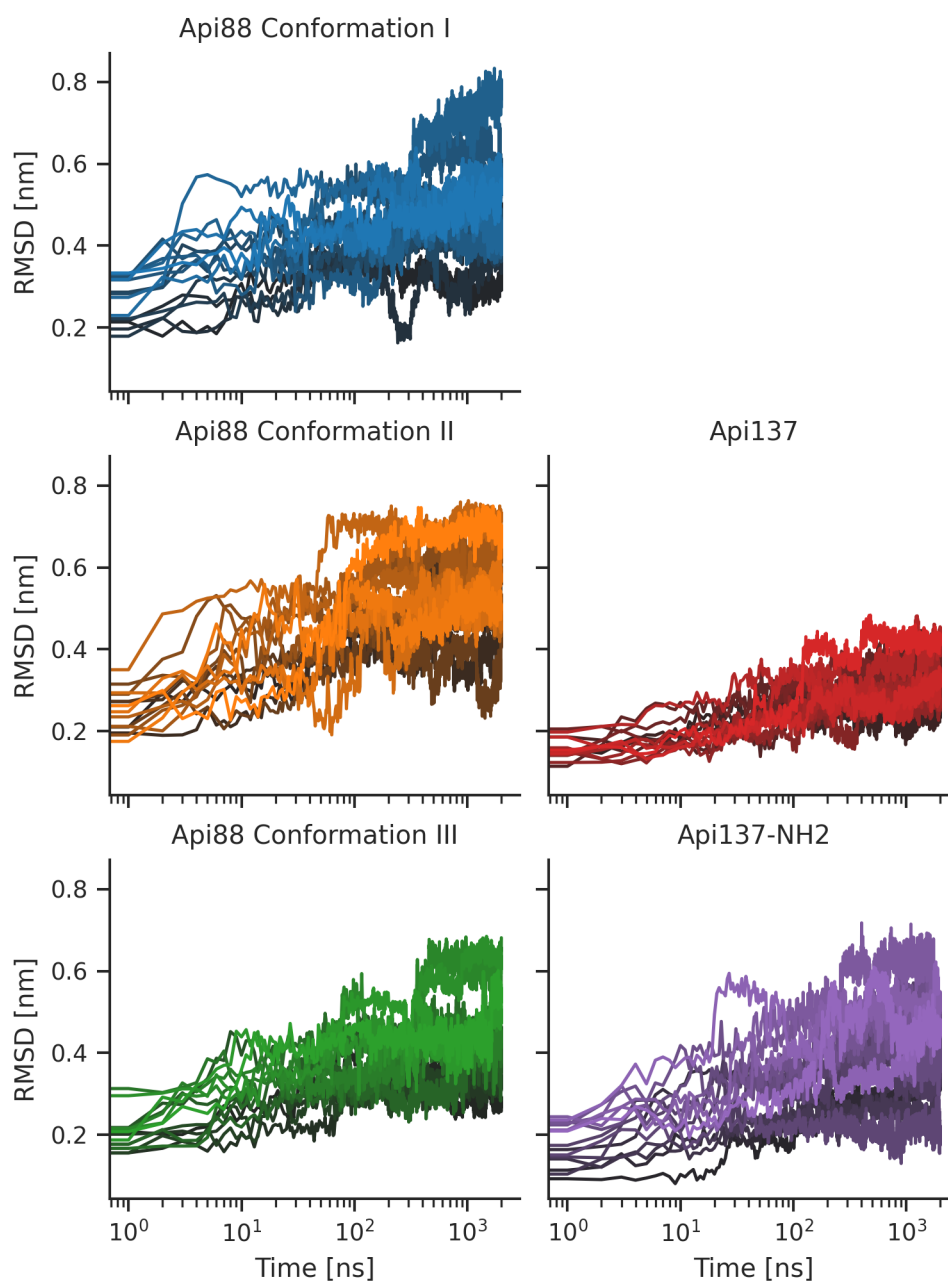


Figure 4.6.: Root mean square deviations of MD snapshots from the starting structures as a function of simulation time. Each time series belongs to one simulation replica (blue: Api88 conformation I, orange: Api88 conformation II, green: Api88 conformation III, red: Api137, purple: Api137-NH2).

4. Results and discussion

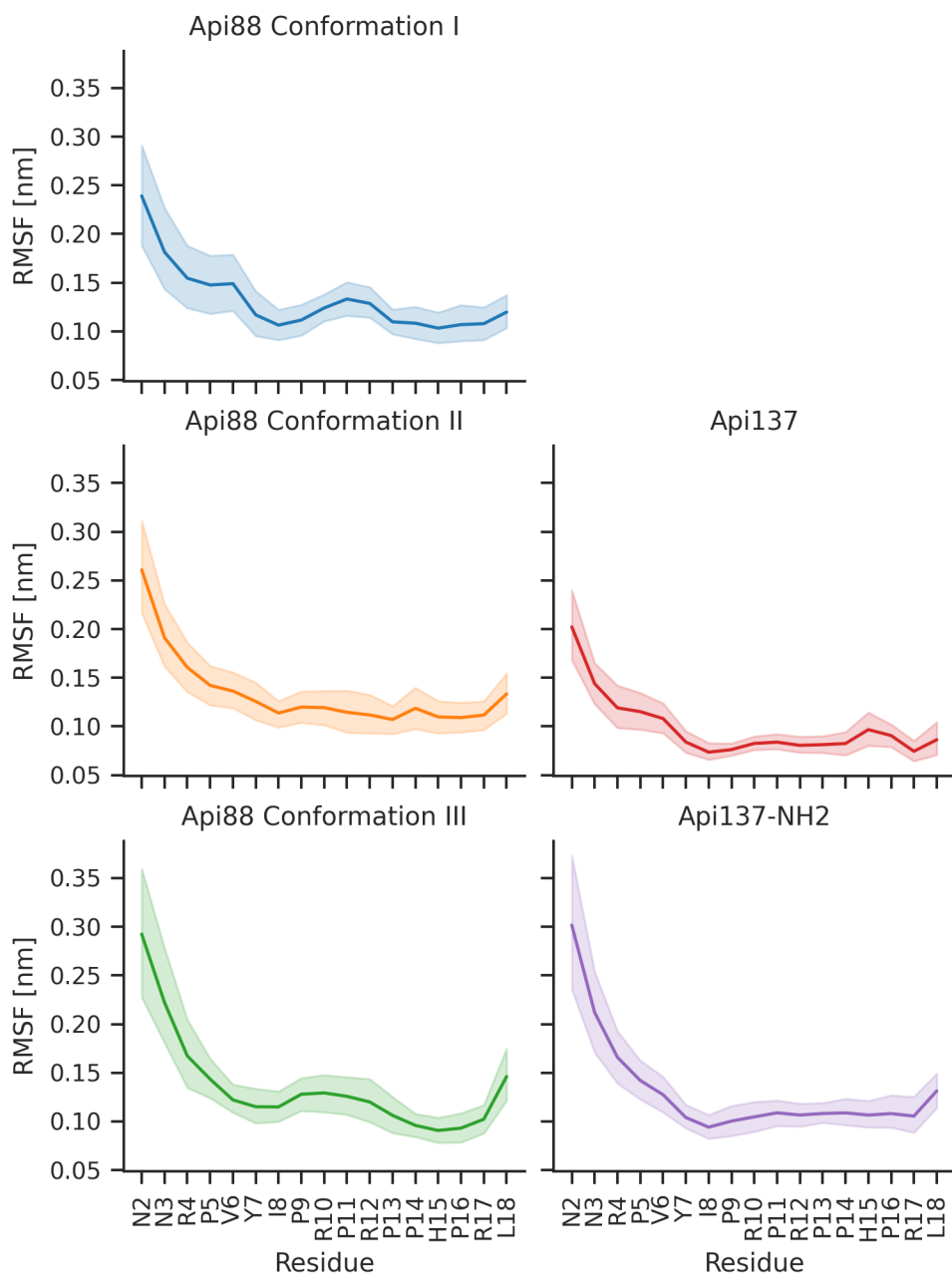


Figure 4.7.: Root mean square fluctuation per residue for all Api88 and Api137 simulations. The thick lines denote mean values, and the shaded areas display 95 % confidence intervals. Mean values and confidence intervals were obtained via bootstrapping of the 15 simulation replicas per starting structure.

4.4. Influence of the C-terminus on binding dynamics of Api88 and Api137

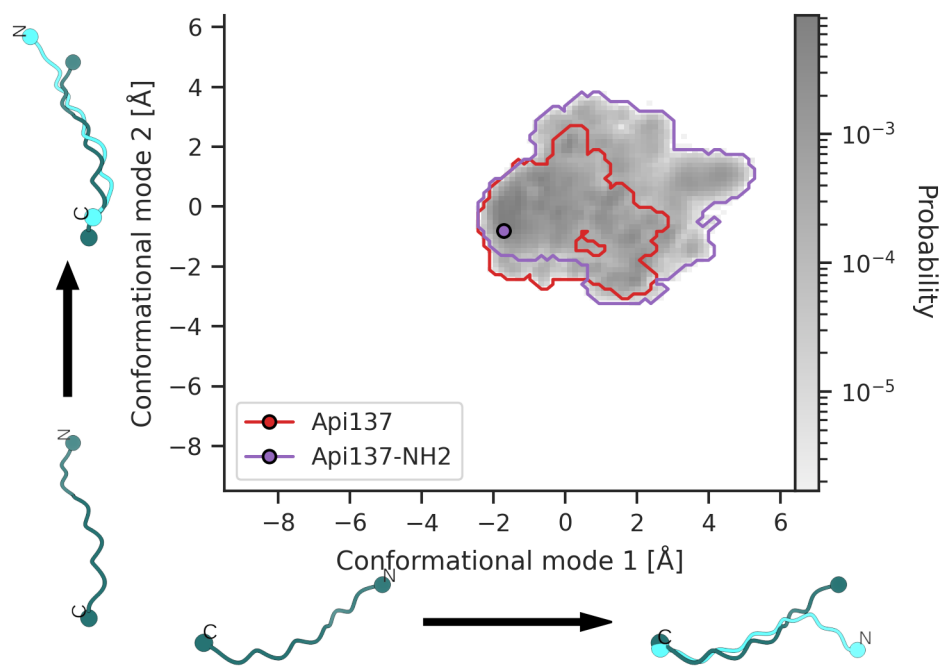


Figure 4.8.: Projections of Api137 and Api137-NH2 trajectories onto their first two principal components. Circles denote the initial structure. The starting points for Api137 and Api137-NH2 overlap because its atomic coordinates are the same.

5. Conclusions and outlook

In this thesis, I complemented the experimental cryo-EM structural data from our collaborators by investigating the binding dynamics of Api88 and Api137 with MD simulations.

I aimed to answer several research questions about the binding dynamics of Api88 and Api137. Three conformations were needed to model the cryo-EM density of Api88 in the exit tunnel and I investigated if the models represent metastable states of the peptide. In addition, I studied how much each of the three conformations contributed to the cryo-EM density, i. e. the probability of each conformation occurring when Api88 binds in the exit tunnel. Further, I inquired if a collection of MD structures of Api88 could describe the cryo-EM density better than the three initial models. Lastly, I compared the binding modes of Api88 and Api137 to elucidate the influence of their chemical difference at the C-terminus.

With PCA I could identify at least two metastable states of Api88. The MD trajectories based on conformation III, which features a C-terminal protrusion towards the PTC compared to the other two model, remain separated from conformation I and II for a time scale of at least 2 ns.

Furthermore, I could elucidate the contribution of each Api88 conformation and their respective MD ensembles to the cryo-EM density. I calculated weights for each Api88 conformation that optimised their correlation to the cryo-EM density. The results highlighted the significance of conformation III in explaining the density with a weight of 0.46. Nevertheless, the contributions of conformations I and II cannot be neglected (weights 0.22 and 0.33). This underscores the necessity of using a conformational ensemble to describe Api88 binding.

I was able to produce additional conformations of Api88 with MD that describe the cryo-EM density better than the initial models. Most of them were shifted toward the PTC, similar to conformation III. This finding supports the notion that PTC-shifted conformations of Api88 occur more frequently than those positioned deeper in the tunnel.

The comparison between the binding dynamics of Api88 and Api137 illustrated the impact of the C-terminal differences. Api137 trajectories showed significantly less flexibil-

5. Conclusions and outlook

ity and a closer resemblance to their starting conformation than Api88 and the amidated variant Api137-NH₂ with the same starting coordinates. The modulation of binding dynamics by the C-terminus agrees with the cryo-EM data. The better-refined density of Api137 already shows that the chemical difference to Api88 impacts the dynamics of the whole peptide.

The precise mechanism of how the C-terminus determines the binding dynamics of Api88 and Api137 remains to be elucidated. It can be hypothesised that changes in electrostatic interactions with the tunnel walls influence the binding of Api88/137, which not only affect the C-terminus but spread down the complete peptide length.

The focus of this work was mainly on extracting additional information about the conformations taken by Api88/Api137, but future studies could focus on the interactions between the peptides and the tunnel walls. It would be interesting to see if the presence of either Api137 or Api88 leads to conformational changes in the RNA and protein residues that make up the tunnel walls.

With more computational power at hand, it might be worthwhile to extend the simulations beyond 2 ns, in order to observe the the movement of Api88 towards the PTC (i. e. the transition from conformation I or II to III). Then, the corresponding energy barrier between the two states could be calculated. Nevertheless, it is unclear if this movement even occurs on time scales that could be simulated with hard- and software available in the near future.

Bibliography

- ¹S. M. Lauer, M. Reepmeyer, O. Berendes, D. Klepacki, J. Gasse, S. Gabrielli, H. Grubmüller, L. V. Bock, A. Krizsan, R. Nikolay, C. M. T. Spahn, and R. Hoffmann, “Multimodal binding and inhibition of bacterial ribosomes by the antimicrobial peptides api137 and api88,” *Nature Communications* **15**, 3945 (2024).
- ²V. M. D’Costa, C. E. King, L. Kalan, M. Morar, W. W. L. Sung, C. Schwarz, D. Froese, G. Zazula, F. Calmels, R. Debruyne, G. B. Golding, H. N. Poinar, and G. D. Wright, “Antibiotic resistance is ancient,” *Nature* **477**, 457–461 (2011).
- ³A. Bahar and D. Ren, “Antimicrobial peptides,” *Pharmaceuticals* **6**, 1543–1575 (2013).
- ⁴M. Graf and D. N. Wilson, “Intracellular antimicrobial peptides targeting the protein synthesis machinery,” in *Antimicrobial peptides*, Vol. 1117, edited by K. Matsuzaki (Springer Singapore, Singapore, 2019), pp. 73–89.
- ⁵A. Krizsan, D. Volke, S. Weinert, N. Sträter, D. Knappe, and R. Hoffmann, “Insect-derived proline-rich antimicrobial peptides kill bacteria by inhibiting bacterial protein translation at the 70 s ribosome,” *Angewandte Chemie International Edition* **53**, 12236–12239 (2014).
- ⁶A. Krizsan, C. Prah, T. Goldbach, D. Knappe, and R. Hoffmann, “Short proline-rich antimicrobial peptides inhibit either the bacterial 70s ribosome or the assembly of its large 50s subunit,” *ChemBioChem* **16**, 2304–2308 (2015).
- ⁷T. Florin, C. Maracci, M. Graf, P. Karki, D. Klepacki, O. Berninghausen, R. Beckmann, N. Vázquez-Laslop, D. N. Wilson, M. V. Rodnina, and A. S. Mankin, “An antimicrobial peptide that inhibits translation by trapping release factors on the ribosome,” *Nature Structural & Molecular Biology* **24**, 752–757 (2017).
- ⁸P. Casteels, C. Ampe, F. Jacobs, M. Vaeck, and P. Tempst, “Apidaecins: antibacterial peptides from honeybees,” *The EMBO journal* **8**, 2387–2391 (1989).

Bibliography

- ⁹P. Czihal, D. Knappe, S. Fritsche, M. Zahn, N. Berthold, S. Piantavigna, U. Müller, S. Van Dorpe, N. Herth, A. Binas, G. Köhler, B. De Spiegeleer, L. L. Martin, O. Nolte, N. Sträter, G. Alber, and R. Hoffmann, “Api88 is a novel antibacterial designer peptide to treat systemic infections with multidrug-resistant gram-negative pathogens,” *ACS Chemical Biology* **7**, 1281–1291 (2012).
- ¹⁰N. Berthold, P. Czihal, S. Fritsche, U. Sauer, G. Schiffer, D. Knappe, G. Alber, and R. Hoffmann, “Novel apidaecin 1b analogs with superior serum stabilities for treatment of infections by gram-negative pathogens,” *Antimicrobial Agents and Chemotherapy* **57**, 402–409 (2013).
- ¹¹L. V. Bock, S. Gabrielli, M. H. Kolář, and H. Grubmüller, “Simulation of complex biomolecular systems: the ribosome challenge,” *Annual Review of Biophysics* **52**, 361–390 (2023).
- ¹²B. Alberts, *Molecular biology of the cell*, Sixth edition (Garland Science, Taylor and Francis Group, New York, NY, 2015).
- ¹³R. H. Garrett and C. M. Grisham, *Biochemistry*, 4. ed., internat. ed (Brooks-Cole, Cengage learning, Boston, Mass., 2010).
- ¹⁴M. Zanetti, L. Litteri, R. Gennaro, H. Horstmann, and D. Romeo, “Bactenecins, defense polypeptides of bovine neutrophils, are generated from precursor molecules stored in the large granules,” *The Journal of cell biology* **111**, 1363–1371 (1990).
- ¹⁵M. Zanetti, L. Litteri, G. Griffiths, R. Gennaro, and D. Romeo, “Stimulus-induced maturation of probactenecins, precursors of neutrophil antimicrobial polypeptides,” *The Journal of Immunology* **146**, 4295–4300 (1991).
- ¹⁶L. Otvos, I. O. M. E. Rogers, P. J. Consolvo, B. A. Condie, S. Lovas, P. Bulet, and M. Blaszczyk-Thurin, “Interaction between heat shock proteins and antimicrobial peptides,” *Biochemistry* **39**, 14150–14159 (2000).
- ¹⁷J. L. S. Milne, M. J. Borgia, A. Bartesaghi, E. E. H. Tran, L. A. Earl, D. M. Schauder, J. Lengyel, J. Pierson, A. Patwardhan, and S. Subramaniam, “Cryo-electron microscopy – a primer for the non-microscopist,” *The FEBS Journal* **280**, 28–45 (2013).
- ¹⁸T. R. Shaikh, H. Gao, W. T. Baxter, F. J. Asturias, N. Boisset, A. Leith, and J. Frank, “SPIDER image processing for single-particle reconstruction of biological macromolecules from electron micrographs,” *Nature Protocols* **3**, 1941–1974 (2008).
- ¹⁹M. Van Heel, G. Harauz, E. V. Orlova, R. Schmidt, and M. Schatz, “A new generation of the IMAGIC image processing system,” *Journal of Structural Biology* **116**, 17–24 (1996).

- ²⁰E. C. Meng, T. D. Goddard, E. F. Pettersen, G. S. Couch, Z. J. Pearson, J. H. Morris, and T. E. Ferrin, “Ucsf chimerax: tools for structure building and analysis,” *Protein Science* **32**, e4792 (2023).
- ²¹P. Emsley, B. Lohkamp, W. G. Scott, and K. Cowtan, “Features and development of *Coot*,” *Acta Crystallographica Section D Biological Crystallography* **66**, 486–501 (2010).
- ²²S. H. W. Scheres and S. Chen, “Prevention of overfitting in cryo-EM structure determination,” *Nature Methods* **9**, 853–854 (2012).
- ²³H. Berendsen, D. Van Der Spoel, and R. Van Drunen, “GROMACS: a message-passing parallel molecular dynamics implementation,” *Computer Physics Communications* **91**, 43–56 (1995).
- ²⁴M. M. Reif, P. H. Hünenberger, and C. Oostenbrink, “New interaction parameters for charged amino acid side chains in the GROMOS force field,” *Journal of Chemical Theory and Computation* **8**, 3705–3723 (2012).
- ²⁵J. A. Maier, C. Martinez, K. Kasavajhala, L. Wickstrom, K. E. Hauser, and C. Simmerling, “Ff14sb: improving the accuracy of protein side chain and backbone parameters from ff99sb,” *Journal of Chemical Theory and Computation* **11**, 3696–3713 (2015).
- ²⁶I. Soteras Gutiérrez, F.-Y. Lin, K. Vanommeslaeghe, J. A. Lemkul, K. A. Armacost, C. L. Brooks, and A. D. MacKerell, “Parametrization of halogen bonds in the CHARMM general force field: improved treatment of ligand–protein interactions,” *Bioorganic & Medicinal Chemistry* **24**, 4812–4825 (2016).
- ²⁷M. J. Robertson, J. Tirado-Rives, and W. L. Jorgensen, “Improved peptide and protein torsional energetics with the OPLS-AA force field,” *Journal of Chemical Theory and Computation* **11**, 3499–3509 (2015).
- ²⁸D. J. Price and C. L. Brooks, “A modified TIP3p water potential for simulation with ewald summation,” *The Journal of Chemical Physics* **121**, 10096–10103 (2004).
- ²⁹K. M. Dyer, J. S. Perkyns, G. Stell, and B. Montgomery Pettitt, “Site-renormalised molecular fluid theory: on the utility of a two-site model of water,” *Molecular Physics* **107**, 423–431 (2009).
- ³⁰J. L. F. Abascal and C. Vega, “A general purpose model for the condensed phases of water: TIP4p/2005,” *The Journal of Chemical Physics* **123**, 234505 (2005).
- ³¹T. Darden, D. York, and L. Pedersen, “Particle mesh ewald: an $N \cdot \log(N)$ method for ewald sums in large systems,” *The Journal of Chemical Physics* **98**, 10089–10092 (1993).

Bibliography

- ³²M. J. Abraham, T. Murtola, R. Schulz, S. Páll, J. C. Smith, B. Hess, and E. Lindahl, “GROMACS: high performance molecular simulations through multi-level parallelism from laptops to supercomputers,” *SoftwareX* **1-2**, 19–25 (2015).
- ³³G. Bussi, D. Donadio, and M. Parrinello, “Canonical sampling through velocity rescaling,” *The Journal of Chemical Physics* **126**, 014101 (2007).
- ³⁴M. Bernetti and G. Bussi, “Pressure control using stochastic cell rescaling,” *The Journal of Chemical Physics* **153**, 114107 (2020).
- ³⁵J. Palma and G. Pierdominici-Sottile, “On the uses of PCA to characterise molecular dynamics simulations of biological macromolecules: basics and tips for an effective use,” *ChemPhysChem* **24**, 10.1002/cphc.202200491 (2023).
- ³⁶B. Hess, “Convergence of sampling in protein simulations,” *Physical Review E* **65**, 031910 (2002).
- ³⁷R. Briones, C. Blau, C. Kutzner, B. L. De Groot, and C. Aponte-Santamaría, “GROMaps: a GROMACS-based toolset to analyze density maps derived from molecular dynamics simulations,” *Biophysical Journal* **116**, 4–11 (2019).
- ³⁸*Root mean square deviations in structure - GROMACS 2024.1 documentation*, <https://manual.gromacs.org/current/reference-manual/analysis/rmsd.html> (visited on 05/06/2024).
- ³⁹*Gmx rmsf - GROMACS 2024.1 documentation*, <https://manual.gromacs.org/current/onlinehelp/gmx-rmsf.html> (visited on 05/06/2024).
- ⁴⁰J. Benesty, J. Chen, Y. Huang, and I. Cohen, “Pearson correlation coefficient,” in I. Cohen, Y. Huang, J. Chen, and J. Benesty, *Noise reduction in speech processing*, Vol. 2 (Springer Berlin Heidelberg, Berlin, Heidelberg, 2009), pp. 1–4.
- ⁴¹E. Gine and J. Zinn, “Bootstrapping general empirical measures,” *The Annals of Probability* **18**, 851–869 (1990).
- ⁴²G. Vriend, “WHAT IF: a molecular modeling and drug design program,” *Journal of Molecular Graphics* **8**, 52–56 (1990).
- ⁴³V. Stojković, A. G. Myasnikov, I. D. Young, A. Frost, J. S. Fraser, and D. G. Fujimori, “Assessment of the nucleotide modifications in the high-resolution cryo-electron microscopy structure of the escherichia coli 50s subunit,” *Nucleic Acids Research* **48**, 2723–2732 (2020).

- ⁴⁴I. S. Joung and T. E. Cheatham, “Determination of alkali and halide monovalent ion parameters for use in explicitly solvated biomolecular simulations,” *The Journal of Physical Chemistry B* **112**, 9020–9041 (2008).
- ⁴⁵K. K. Grotz and N. Schwierz, “Magnesium force fields for OPC water with accurate solvation, ion-binding, and water-exchange properties: successful transfer from SPC/e,” *The Journal of Chemical Physics* **156**, 114501 (2022).
- ⁴⁶S. Izadi, R. Anandakrishnan, and A. V. Onufriev, “Building water models: a different approach,” *The Journal of Physical Chemistry Letters* **5**, 3863–3871 (2014).
- ⁴⁷M. Abraham, A. Alekseenko, C. Bergh, C. Blau, E. Briand, M. Doijade, S. Fleischmann, V. Gapsys, Gaurav Garg, S. Gorelov, G. Gouaillardet, A. Gray, M. Eric Irrgang, F. Jalaly-pour, J. Jordan, C. Junghans, Prashanth Kanduri, S. Keller, C. Kutzner, J. A. Lemkul, M. Lundborg, P. Merz, V. Miletic, D. Morozov, S. Páll, R. Schulz, M. Shirts, A. Shvetsov, B. Soproni, D. Van Der Spoel, P. Turner, C. Uphoff, A. Villa, S. Wingbermühle, A. Zhmurov, P. Bauer, B. Hess, and E. Lindahl, “GROMACS 2023 manual,” 10.5281/ZENODO.7588711 (2023).
- ⁴⁸P. Huter, S. Arenz, L. V. Bock, M. Graf, J. O. Frister, A. Heuer, L. Peil, A. L. Starosta, I. Wohlgemuth, F. Peske, J. Nováček, O. Berninghausen, H. Grubmüller, T. Tenson, R. Beckmann, M. V. Rodnina, A. C. Vaiana, and D. N. Wilson, “Structural basis for polyproline-mediated ribosome stalling and rescue by the translation elongation factor EF-p,” *Molecular Cell* **68**, 515–527.e6 (2017).
- ⁴⁹S. Arenz, L. V. Bock, M. Graf, C. A. Innis, R. Beckmann, H. Grubmüller, A. C. Vaiana, and D. N. Wilson, “A combined cryo-EM and molecular dynamics approach reveals the mechanism of ErmBL-mediated translation arrest,” *Nature Communications* **7**, 12026 (2016).
- ⁵⁰G. v. Rossum and F. L. Drake, *The python language reference*, Release 3.0.1 [Repr.], Python documentation manual / Guido van Rossum; Fred L. Drake [ed.] Pt. 2 (Python Software Foundation, Hampton, NH, 2010), 109 pp.
- ⁵¹Schrodinger, “The PyMOL molecular graphics system, version 1.8,” Nov. 2015.
- ⁵²P. Virtanen, R. Gommers, T. E. Oliphant, M. Haberland, T. Reddy, D. Cournapeau, E. Burovski, P. Peterson, W. Weckesser, J. Bright, S. J. Van Der Walt, M. Brett, J. Wilson, K. J. Millman, N. Mayorov, A. R. J. Nelson, E. Jones, R. Kern, E. Larson, C. J. Carey, Í. Polat, Y. Feng, E. W. Moore, J. VanderPlas, D. Laxalde, J. Perktold, R. Cimrman, I. Henriksen, E. A. Quintero, C. R. Harris, A. M. Archibald, A. H. Ribeiro, F. Pedregosa,

Bibliography

P. Van Mulbregt, SciPy 1.0 Contributors, A. Vijaykumar, A. P. Bardelli, A. Rothberg, A. Hilboll, A. Kloeckner, A. Scopatz, A. Lee, A. Rokem, C. N. Woods, C. Fulton, C. Masson, C. Häggström, C. Fitzgerald, D. A. Nicholson, D. R. Hagen, D. V. Pasechnik, E. Olivetti, E. Martin, E. Wieser, F. Silva, F. Lenders, F. Wilhelm, G. Young, G. A. Price, G.-L. Ingold, G. E. Allen, G. R. Lee, H. Audren, I. Probst, J. P. Dietrich, J. Silterra, J. T. Webber, J. Slavič, J. Nothman, J. Buchner, J. Kulick, J. L. Schönberger, J. V. De Miranda Cardoso, J. Reimer, J. Harrington, J. L. C. Rodríguez, J. Nunez-Iglesias, J. Kuczynski, K. Tritz, M. Thoma, M. Newville, M. Kümmerer, M. Bolingbroke, M. Tartre, M. Pak, N. J. Smith, N. Nowaczyk, N. Shebanov, O. Pavlyk, P. A. Brodtkorb, P. Lee, R. T. McGibbon, R. Feldbauer, S. Lewis, S. Tygier, S. Sievert, S. Vigna, S. Peterson, S. More, T. Pudlik, T. Oshima, T. J. Pingel, T. P. Robitaille, T. Spura, T. R. Jones, T. Cera, T. Leslie, T. Zito, T. Krauss, U. Upadhyay, Y. O. Halchenko, and Y. Vázquez-Baeza, “SciPy 1.0: fundamental algorithms for scientific computing in python,” *Nature Methods* **17**, 261–272 (2020).

A. PCA of Api88 trajectories

A. PCA of A π i88 trajectories

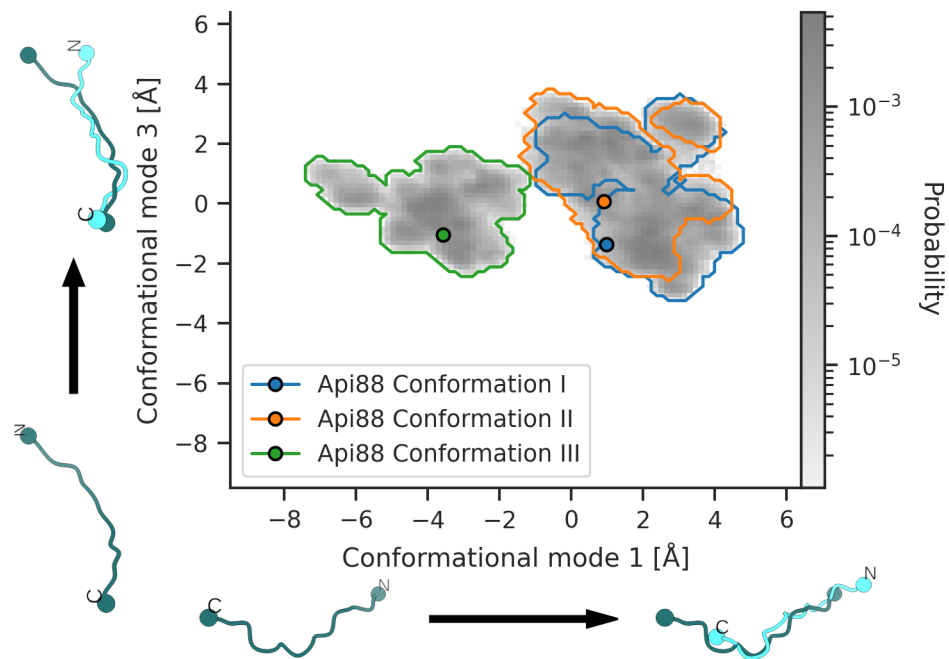


Figure A.1.: Projection of A π i88 trajectories onto conformational modes 1 and 3

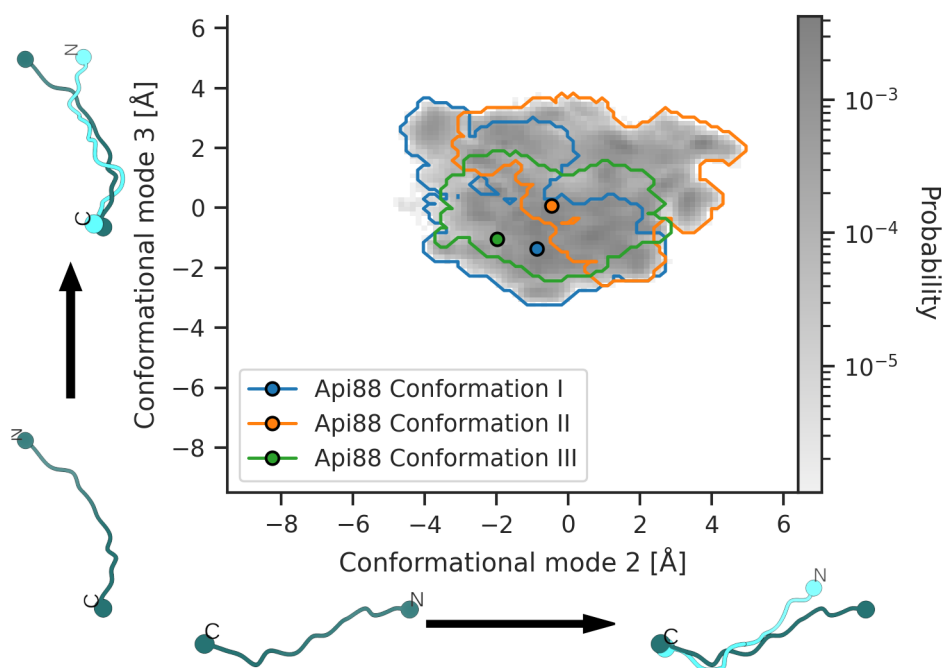


Figure A.2.: Projection of A π i88 trajectories onto conformational modes 2 and 3

B. PCA of Api137 trajectories

B. PCA of Api137 trajectories

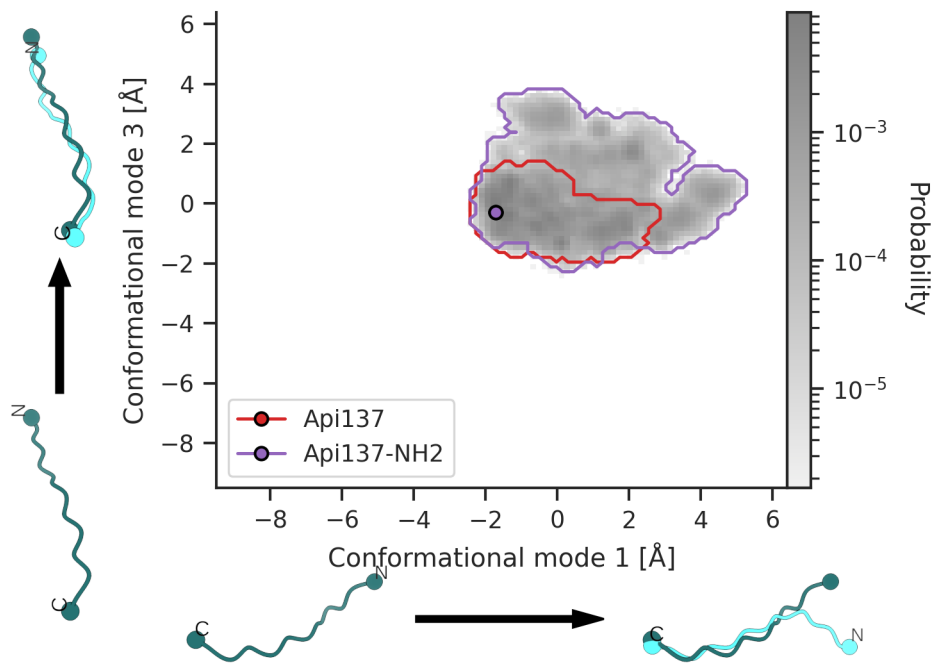


Figure B.1.: Projection of Api137 trajectories onto conformational modes 1 and 3

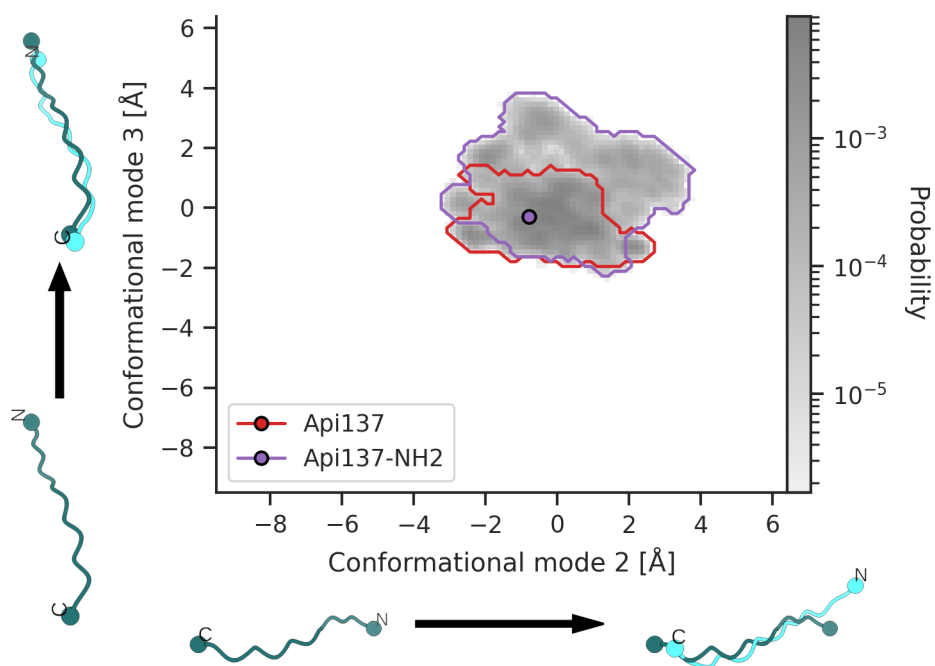


Figure B.2.: Projection of Api137 trajectories onto conformational modes 2 and 3

C. PCA of combined Api88 and Api137 trajectories

C. PCA of combined Api88 and Api137 trajectories

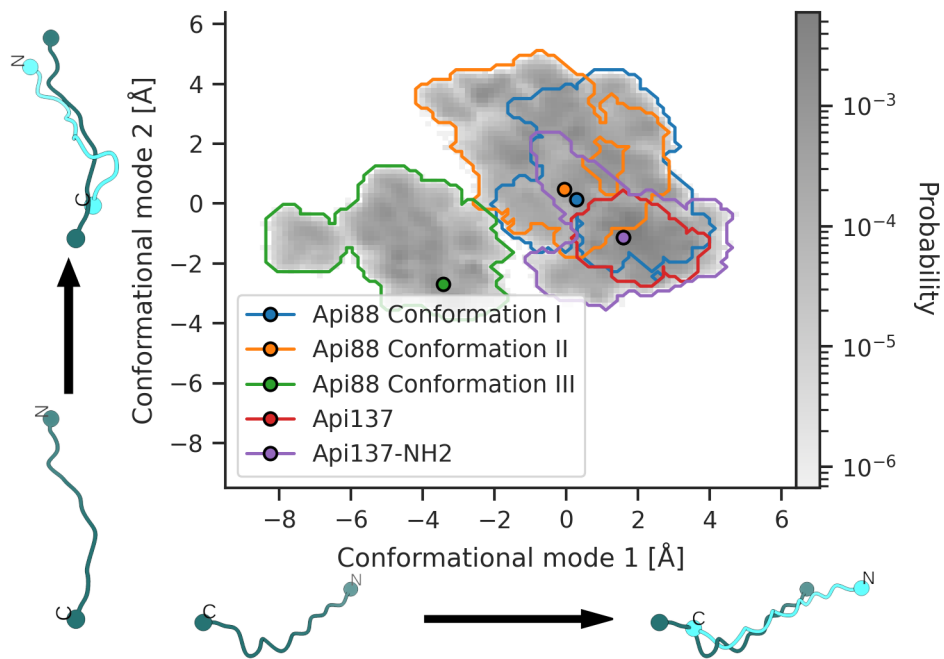


Figure C.1.: Projection of Api137 trajectories onto conformational modes 1 and 2

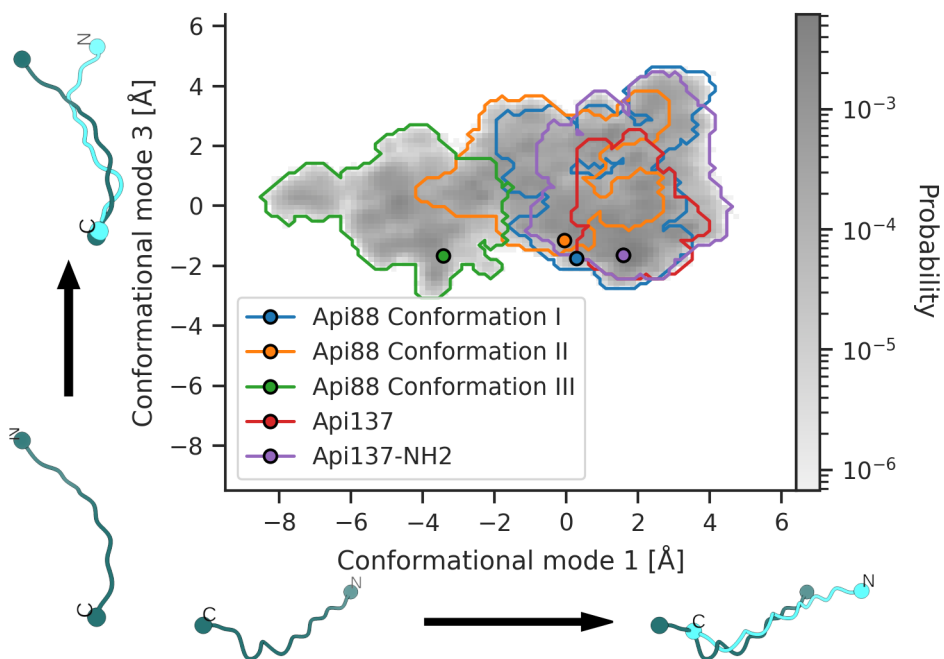


Figure C.2.: Projection of Api137 trajectories onto conformational modes 1 and 3

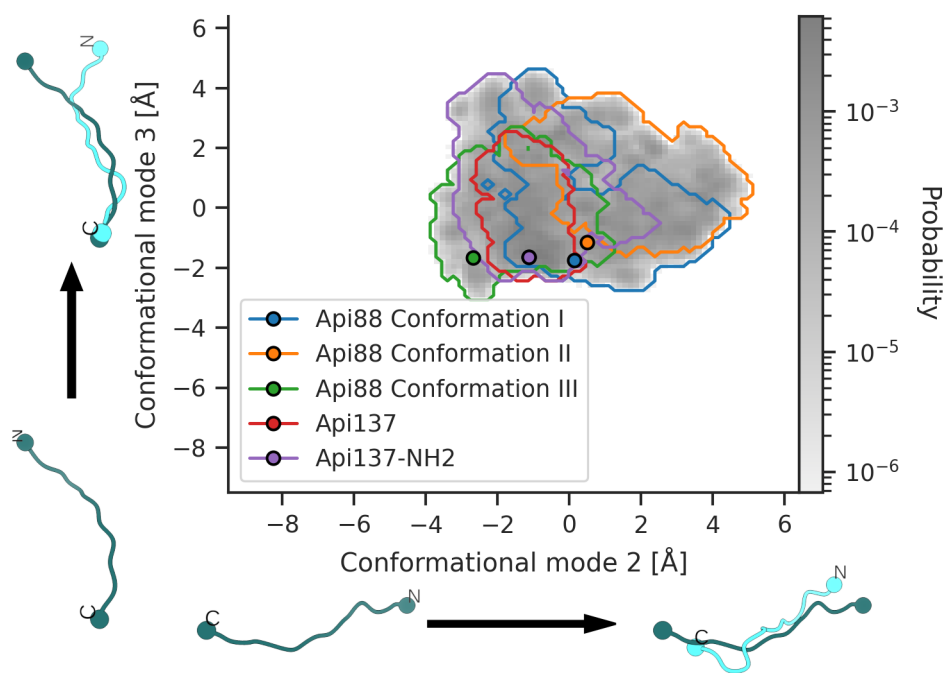


Figure C.3.: Projection of Api137 trajectories onto conformational modes 2 and 3

Erklärung

Ich versichere hiermit, dass ich die vorliegende Arbeit ohne fremde Hilfe selbstständig verfasst und nur die von mir angegebenen Quellen und Hilfsmittel verwendet habe. Wörtlich oder sinngemäß aus anderen Werken entnommene Stellen habe ich unter Angabe der Quellen kenntlich gemacht. Die Richtlinien zur Sicherung der guten wissenschaftlichen Praxis an der Universität Göttingen wurden von mir beachtet. Eine gegebenenfalls eingereichte digitale Version stimmt mit der schriftlichen Fassung überein. Mir ist bewusst, dass bei Verstoß gegen diese Grundsätze die Prüfung mit nicht bestanden bewertet wird.

Göttingen, den 2. August 2024

(Ole Berendes)